J. Fluid Mech. (2025), *vol.* 1017, A33, doi:10.1017/jfm.2025.369

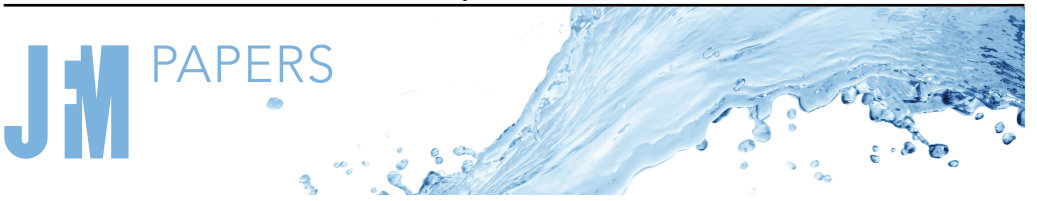

Hypersonic boundary-layer transition over a circular cone in a Mach 8 digital wind tunnel

Mateus Schuabb[1], Lian Duan[1], Katya M. Casper[2], Ross M. Wagnild[3], Meelan M. Choudhari[4] and Pedro Paredes[4]

[1]Department of Mechanical and Aerospace Engineering, The Ohio State University, Columbus, OH 43210, USA

[2]Experimental Aerosciences Department, Sandia National Laboratories, Albuquerque, NM 87185, USA

[3]Computational Aerosciences Department, Sandia National Laboratories, Albuquerque, NM 87185, USA

[4]Computational AeroSciences Branch, NASA Langley Research Center, Hampton, VA 23681, USA

Corresponding author: Lian Duan, duan.322@osu.edu

(Received 25 September 2024; revised 4 February 2025; accepted 14 March 2025)

In conventional hypersonic wind tunnels, tunnel noise is dominated by acoustic radiation from turbulent nozzle-wall boundary layers, which can directly influence the boundary-layer transition (BLT) over the model in the test section. To offer new insights into BLT in conventional ground facilities, direct numerical simulations (DNS) were performed to simulate the receptivity and transition processes of a Mach 8 boundary layer over a nearly sharp 7° half-angle cone, with transition triggered by tunnel-like broadband free-stream acoustic disturbances radiated from the nozzle wall of the Sandia hypersonic wind tunnel at Mach 8 (Sandia HWT-8). The DNS captured all the stages of the transition to turbulence caused by tunnel noise, including the passage of broadband free-stream noise through the shock wave, the receptivity process leading to the generation of Mack's second-mode waves, their nonlinear growth to saturation, the laminar breakdown to turbulence and the post-transitional, fully turbulent flow. The transition location predicted by DNS compared well with that of Pate's theory and was also consistent with the locations of peak pressure fluctuations as measured in the Sandia HWT-8 facility. The computed skin friction and Stanton number distributions in the initial breakdown region showed an overshoot compared with the turbulent predictions by the van Driest II theory. The wall-pressure spectra in both the transitional and turbulent regions of the cone compared well with those measured in the Sandia HWT-8. The second-mode breakdown amplitude A_{max}

predicted by the DNS was also consistent with sharp-cone measurements from multiple conventional wind tunnels.

Key words: boundary layer receptivity, hypersonic flow, compressible boundary layers

1. Introduction

Accurate prediction of boundary-layer transition (BLT) is essential to the design of hypersonic thermal protection systems. However, our ability to predict transition during hypersonic flight is hindered by the high levels of acoustic noise in most hypersonic ground-test facilities (Beckwith & Miller 1991; Schneider 2001). There are few existing quiet hypersonic wind tunnels, and these tunnels are limited to Mach 6, moderate Reynolds numbers, low free-stream enthalpy and subscale models (Schneider 2008). While plans are being formulated for the long, expensive process of constructing new, quiet hypersonic wind tunnels, rapid progress in the field of hypersonic BLT would be possible in the near term via improved understanding of data obtained from conventional (i.e. noisy) wind tunnels.

In a low-enthalpy hypersonic wind tunnel with adequate flow conditioning, the free-stream disturbance environment is dominated by acoustic radiation from tunnel-wall turbulent boundary layers (Laufer 1961, 1964; Pate 1978; Stetson 1983; Bushnell 1990). Tunnel noise can impact not only the transition location, but possibly the transition mechanism as well. The effect of tunnel noise on transition cannot be quantified in terms of a single metric that corresponds to the root-mean-square (r.m.s.) amplitude, as indicated by the measurements at Purdue University (Schneider 2001). For the second-mode instability in particular, given its acoustic nature, its space and time scales can coincide with those of typical acoustic waves in the free stream (Fedorov 2011). Thus, hypersonic BLT is particularly sensitive to the detailed spectrum of free-stream acoustic noise. Experiments in the Purdue quiet tunnel have shown that tunnel noise has a dramatic effect on the nonlinear breakdown of second-mode waves (Schneider 2015; Edelman *et al.* 2016). Specifically, there is a large discrepancy in the breakdown amplitude of second-mode waves between data obtained in a quiet tunnel versus that in the conventional facilities (Edelman *et al.* 2016). Such an influence is hard to quantify however because the Reynolds number limitation of the quiet tunnels often prevents a fully turbulent flow in the facility.

To date, most studies of the interaction of free-stream acoustic disturbances with a laminar boundary layer (referred to as boundary-layer receptivity) in the hypersonic regime have been carried out by either assuming the incoming free-stream disturbance field to be comprised of a deterministic train of plane acoustic waves (Zhong & Ma 2006; Balakumar & Chou 2018), or by using a random inflow forcing across a broad range of frequencies and wavenumbers (Hader & Fasel 2018; Ran *et al.* 2019; Goparaju *et al.* 2021). For instance, Ma & Zhong (2003) reported the response of a Mach 4.5 flow to inflow disturbances that are taken from one-dimensional linear analyses. Balakumar & Kegerise (2015) and Balakumar & Chou (2016) examined the response of hypersonic boundary layers to acoustic waves described by *ad hoc* analytical expressions. Although these computational works have clarified a number of receptivity mechanisms responsible for the excitation of instability waves in high-speed boundary layers (see, for instance, the reviews by Fedorov (2011) and Zhong & Wang (2012)), they pertain almost exclusively to time-harmonic (i.e. purely deterministic) free-stream disturbances and cannot be directly applied to explain the observed effect of tunnel-flow quality on transition. To help bridge the gap between receptivity computations and experiments in conventional wind tunnels, Balakumar & Chou (2018) made an attempt to predict transition onset in the flow over

a 7° half-angle straight cone at Mach 10 by using the measured spectrum of free-stream acoustic disturbances. However, only two-dimensional (2-D), planar acoustic waves were imposed in the simulations, unlike the three-dimensional (3-D) noise field radiated from the nozzle walls that impinges on a test article at oblique angles. Balakumar *et al.* (2018) further examined the response of a Mach 3.5 flow over a sharp, 7° half-angle cone to oblique acoustic waves described by assumed analytical expressions. Their study was largely focused on the receptivity to free-stream acoustic disturbances in the pre-transitional regime, and the physics of nonlinear breakdown of instability waves and the subsequent turbulent flow was excluded. As far as nonlinear transition physics is concerned, there are no existing studies to provide a clarification of the effects of tunnel noise on the natural nonlinear breakdown of instability waves (Schneider 2015). As a result, it is often difficult to relate the noisy tunnel measurements of breakdown features such as hot streaks and skin-friction overshoots to BLT in flight.

Direct numerical simulations (DNS) are now offering new insights into the acoustic noise emanating from the turbulent boundary layer over the nozzle walls of conventional ground facilities (Duan *et al.* 2019*a*,*b*; Hildebrand *et al.* 2022, 2023). For instance, Duan *et al.* (2019*a*,*b*) and Hildebrand *et al.* (2022, 2023) simulated the free-stream acoustic disturbances via DNS of the full-scale nozzles of the Mach 6 Ludwieg tube at the Technical University of Braunschweig (HLB), NASA's 20-in. Mach 6 wind tunnel and the Sandia hypersonic wind tunnel at Mach 8 (Sandia HWT-8). These DNS were shown to successfully capture the physics of noise generation inside the turbulent nozzle-wall boundary layer and provided multipoint statistics to characterise the spatiotemporal structure of the free-stream noise. The noise spectra predicted by the DNS achieved encouraging agreement with those measured in the experiments. These simulations have established the foundation for a 'virtual' testing of the hypersonic BLT in a digital wind tunnel, and also provided the basis for the current work.

The objective of this paper is to numerically characterise the effect of broadband free-stream acoustic disturbances typical of a conventional hypersonic wind tunnel on boundary-layer instability and transition over a nominally sharp 7° half-angle circular cone at zero angle of attack. The flow conditions and cone geometry represent those used in the Sandia HWT-8, which is a conventional hypersonic wind tunnel. To generate the 'tunnel-like' free-stream acoustic disturbances, a precursor DNS of acoustic radiation from turbulent nozzle-wall boundary layers has been conducted at the experimental conditions of the Sandia HWT-8 (Duan *et al.* 2019*b*). The broadband free-stream disturbances radiated from the nozzle wall are then extracted and imposed at the outer boundary of the cone DNS. To establish a holistic approach of simulating natural transition in conventional hypersonic wind tunnels, the cone DNS has taken into account all stages within transition, including receptivity, linear and nonlinear evolution of instability waves and laminar breakdown, and the numerical results are validated by directly comparing with experiments at the Sandia HWT-8 (Casper *et al.* 2016; Smith *et al.* 2016). The study contributes an improved knowledge base for receptivity in a broadband disturbance environment, which would help determine the effects of tunnel noise on the nonlinear transition physics at Mach 8, including the nonlinear evolution and breakdown of second-mode waves and the associated N-factors at transition.

The paper is structured as follows. Section 2 outlines the flow conditions and numerical details for the cone simulation, which includes the methodology of extracting and reconstructing the tunnel-like acoustic disturbances from a precursor DNS of acoustic radiation from a turbulent nozzle-wall boundary layer. Section 3 presents the numerical results of a sharp 7° half-angle cone, including (i) the quantification of initial amplitudes and spectra of the second-mode instability waves that are excited by the tunnel noise, and

$Re_{\infty,1}$ (m^{-1})	$M_{\infty,1}$	$p_{\infty,1}$ (Pa)	$T_{\infty,1}$ (K)	$M_{\infty,2}$	$p_{\infty,2}$ (Pa)	$T_{\infty,2}$ (K)	T_w (K)
12.2×10^6	8.08	448.80	43.90	7.07	1010.02	56.14	298

Table 1. Preshock and postshock free-stream conditions for DNS of a Mach 8 cone.

(ii) an investigation of the nonlinear flow physics associated with laminar breakdown and a naturally generated turbulent boundary layer over the sharp 7° cone within the tunnel-noise field. Section 4 summarises the findings from the study and presents the conclusions.

2. Flow conditions and DNS methodology

The DNS of a hypersonic boundary layer in a synthetic but tunnel-like disturbance environment were conducted for a 0.56-m-long, 7° half-angle axisymmetric cone with a sharp nose radius of 0.5 mm. To simulate BLT within a digital wind tunnel, a precursor DNS of the full-scale, empty axisymmetric nozzle of the conventional Sandia HWT-8 was first conducted at a nominal operational condition of total pressure of $P_0 \approx 4692$ kPa and a total temperature of $T_0 \approx 617$ K. The flow conditions, including the unsteady acoustic disturbances at the centre of the nozzle near the nozzle exit plane, were extracted and used for the main simulation including the cone. More details of the precursor DNS of the digital wind tunnel along with the methodology for extracting free-stream acoustic disturbances were introduced in Liu *et al.* (2022), which are repeated in Appendix A for completeness.

Table 1 summarises the extracted mean free-stream conditions used for the DNS with the cone. The free-stream conditions fall within the range of the cone experiments reported in Casper *et al.* (2016) and Smith *et al.* (2016). At a selected unit Reynolds number of $Re_{\infty,1} = 12.2 \times 10^6$ m^{-1}, experiments have confirmed that the aft portion of the cone ($x_g \gtrsim 0.3$ m) was under a fully turbulent boundary layer (Casper *et al.* 2016), where x_g is the axial distance from the sharp nose. The wall temperature of the cone was set to 298 K, consistent with the experimental set-up, corresponding to a wall-to-recovery temperature ratio of $T_w/T_r \approx 0.54$. Here, the recovery temperature T_r is given by $T_r = T_{\infty,2}(1 + r(\gamma - 1)M^2_{\infty,2}/2)$, with a turbulent recovery factor of $r = 0.89$. At the given Mach number and wall temperature, the degree of wall cooling effects is expected to be small at least in the post-transitional regime, according to a recent classification of wall cooling effects based on the Eckert number by Gibis *et al.* (2024). Throughout this paper, pre-shock free-stream quantities are denoted by $(\cdot)_{\infty,1}$, while the post-shock free-stream quantities are denoted by $(\cdot)_{\infty,2}$ and are calculated using the inviscid Taylor–Maccoll relation (assuming a hypothetical irrotational, inviscid flow over the cone). While the free-stream and wall-temperature conditions were similar to those of the cone experiment in the Sandia HWT-8, the cone length of 0.56 m in the DNS was longer than the experimental model length of 0.517 m. The longer cone length in the DNS ensured that the current DNS captures a larger portion of the post-transitional region of the cone boundary layer, enabling the study of turbulence statistics in regions of both nascent and fully developed, equilibrium turbulence. Given that the cone model was not included in the precursor wind-tunnel simulation, the increase in the cone length for the current DNS will not lead to any adverse pressure-gradient effects due to the blocking of the tunnel test section. On the other hand, the larger nose radius of 0.5 mm in the DNS (in comparison to 0.05 mm in the experiment) alleviated the time-step limitation due to the very fine grid required near the nose of the cone. As will be shown in § 2.3, the small mismatch in R_n between the DNS and experiment does not lead to a significant change in the instability characteristics,

and therefore, the instability and transition should remain second-mode-dominated even for $R_n = 0.5$ mm.

2.1. *Governing equations and numerical methods*

To simulate the turbulent boundary layer on a circular cone (including the nose tip), the full 3-D compressible Navier–Stokes equations in conservation form were solved numerically in cylindrical coordinates. The singularity at the polar axis, as manifested in the $1/r$ terms of the governing equations, was handled by shifting the grid points in the radial direction by one-half of the mesh spacing, following the approach proposed by Mohseni & Colonius (2000). In this approach, less accurate one-sided finite difference evaluation of radial derivatives close to the pole ($r = 0$) is eliminated by mapping the flow domain from $(0, R) \times (0, 2\pi)$ to $(-R, R) \times (0, \pi)$, where R is the radius of the computational domain.

The working fluid in the Sandia HWT-8 facility was nitrogen and the flow conditions fall within the perfect gas regime with an ideal gas constant of $R = 296.7\ \mathrm{J\,(K\,kg)^{-1}}$. The usual constitutive relations for a Newtonian fluid were used: the viscous stress tensor was linearly related to the rate-of-strain tensor and the heat-flux vector was linearly related to the temperature gradient through Fourier's law. The coefficient of viscosity μ was computed from Keyes law (Keyes 1951) and the coefficient of thermal conductivity κ was computed from $\kappa = \mu C_p/Pr$, with a molecular Prandtl number of $Pr = 0.71$. The inviscid fluxes of the governing equations were computed using a fifth-order weighted essentially non-oscillatory (WENO) scheme (Jiang & Shu 1996), which is similar to the previous receptivity DNS performed by Balakumar *et al.* (2018). In order to achieve a more accurate resolution of the imposed free-stream acoustic field and the induced instability waves within the cone boundary layer, the optimal stencil of the WENO scheme was used within most of the free stream and in the pre-transitional region of the boundary layer, while WENO adaptation is only turned on in the immediate vicinity of the shock and within the breakdown and turbulent portions of the cone boundary layer, which is required for capturing the leading-edge shock of the cone as well as eddy shocklets that can appear in the breakdown and turbulent portions of the boundary layer, where there are strong enough fluctuations so that the instantaneous value of the local Mach number exceeds unity. The viscous fluxes were discretised using a fourth-order central difference scheme, and time integration was performed using a third-order low-storage Runge-Kutta scheme (Williamson 1980). The time step limitation due to reduced azimuthal spacing in the vicinity of the centreline (or pole) was addressed by dropping 64, 32, 16, 8, 8, 8, 8, 4, 4 and 4 points in the first 10 azimuthal grid circles with the smallest r (that is, $r = (n - 1/2)\Delta r$ $(n = 1, 2, \ldots, 10)$), which led to an effective azimuthal mesh spacing of $(r\Delta\theta)^+ = 0.0057, 0.037, 0.072, 0.083, 0.15, 0.25, 0.39, 0.28, 0.38, 0.50$, respectively, at $n = 1, 2, \ldots, 10$. A similar approach has been used by Bogey *et al.* (2011) for computing derivatives in the azimuthal direction θ when flow equations are solved in cylindrical coordinates using finite differences.

The details of the DNS methodology have been documented in our previous simulations for axisymmetric wind-tunnel nozzles and circular cones (Huang *et al.* 2017*a*,*b*; Duan *et al.* 2019*a*,*b*; Liu *et al.* 2022; Schuabb *et al.* 2024).

2.2. *Simulation set-up and boundary conditions*

To numerically investigate the transitional and turbulent boundary layer over a circular cone that is subject to tunnel-like free-stream acoustic disturbances, the DNS was set up with the outer top boundary of the computational domain lying outside the leading-edge

shock of the cone. Tunnel-like free-stream acoustic disturbances were then introduced by prescribing flow variables at this boundary based on the data saved from the precursor DNS of the disturbance environment inside a digital wind tunnel that pertains to an empty wind-tunnel configuration (i.e. without the test article). Fluctuation data within the free-stream region of the precursor DNS were extracted and reconstructed as the superposition of a large number of plane slow-acoustic-wave components (A1), fed through the outer boundary of the computational domain of the DNS involving the cone (see Appendix A for details of the tunnel-noise extraction process). Given the small nose radius of the nearly sharp cone, a very fine grid is used in the vicinity of the nose tip, which limits the allowable time step in that region. Since this constraint is entirely due to stability constraints of the numerical scheme, the cone DNS was conducted in multiple stages involving five overlapping streamwise domains as schematically shown in figure 1. The computation of box 1 was done near the nose region, with a very small time step (referred to as box 1 DNS). For downstream boxes, wherein larger time steps can be used to evolve the boundary-layer disturbances internalised within the upstream region, the inflow conditions were prescribed using the data saved and interpolated from the upstream DNS box. As visualised in figure 1, a small overlapping region exists between neighbouring boxes to avoid any numerical effects from the outlet boundary condition into the inflow of the next downstream box. This overlap region also allows one to check and confirm the smooth continuation of the flow field between two neighbouring boxes (i.e. to guarantee the exact match of the flow solutions in such a region). A multidomain simulation approach of this type was previously applied to the DNS of BLT over a cone (Balakumar & Kegerise 2015; Balakumar & Chou 2016; Huang *et al.* 2024). On the wall, no-slip conditions are applied for the three velocity components and an isothermal condition is used for the temperature. At the outlet boundary for each box, unsteady non-reflecting boundary conditions based on Thompson (1987) are imposed to avoid acoustic reflections at the boundary. As illustrated in figure 1, the entire circumference of the cone, 2π rad, was considered for the azimuthal domain, and periodic boundary conditions were used in the azimuthal direction. The outer top boundary conformed to the shape of the leading-edge shock with a slightly larger opening angle of approximately 13° than the shock angle of 10.27° over the cone frustum and, as mentioned previously, was placed outside of the leading-edge shock of the cone across all the boxes, and a Dirichlet boundary condition based on the free-stream acoustic disturbance data saved from the precursor tunnel DNS was imposed. Note that the pre-shock free-stream acoustic disturbances were modelled by the superposition of plane slow acoustic waves and, therefore, had no vortical and entropic contents. However, vortical and entropic components can be generated post shock by the interaction of the acoustic disturbances with the shock wave (McKenzie & Westphal 1968; Mahesh *et al.* 1995; Liu & Duan 2022).

To minimise the initial transient due to the formation of the leading-edge shock, a 2-D axisymmetric laminar baseflow of the cone was first computed and used as the initial condition for the 3-D DNS that includes the full circumference of the cone. Figure 2 shows the comparison between the laminar baseflow solution computed by the WENO-based DNS code and the second-order finite-volume VULCAN flow solver from NASA (Litton *et al.* 2003). Results are presented for the pressure contours as well as boundary-layer profiles for selected flow variables. Excellent agreement was observed between the current DNS and those from VULCAN.

The details of the grid dimensions, domain size and resolutions of the cone DNS are listed in table 2. Here, N_x, N_θ and N_r denote the number of grid points in the streamwise, azimuthal and radial directions, respectively. The range of x_g indicates the streamwise

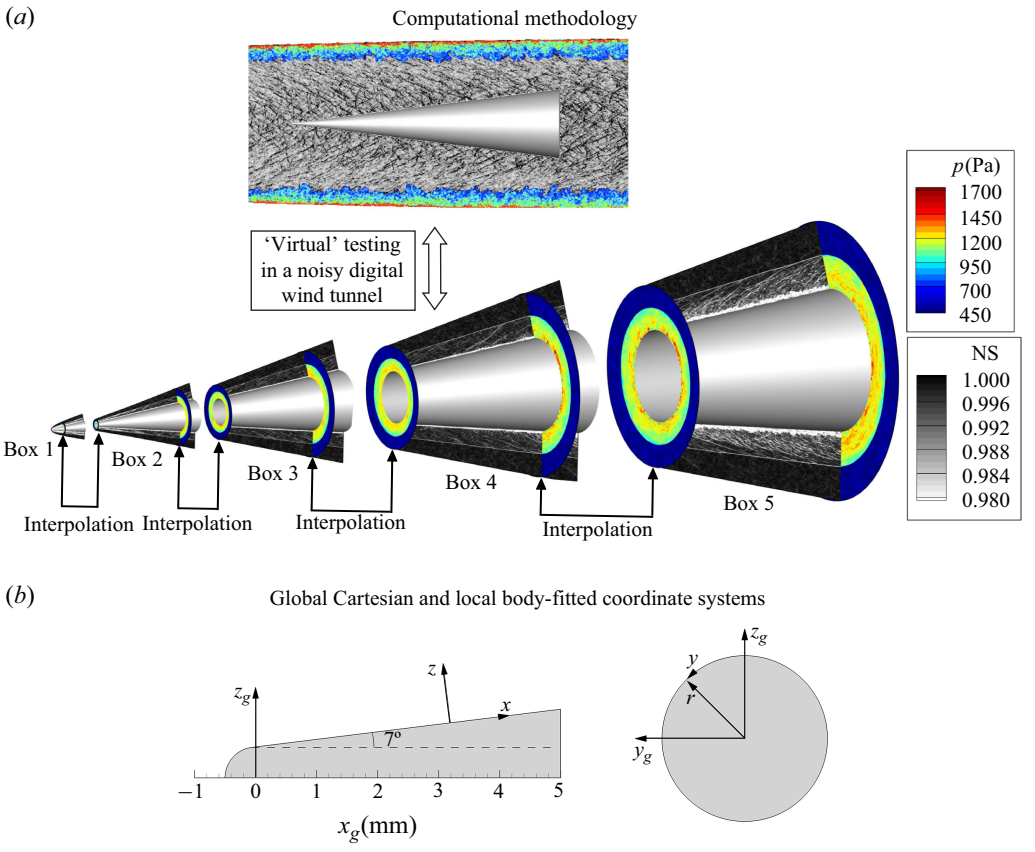

Figure 1. Computational domain and simulation set-up for DNS of Mach 8 flow over a 7° half-angle circular cone with a nose radius of $R_n = 0.5$ mm. The contour plots are generated by overlaying the numerical schlieren ($NS = \exp(-10|\nabla\rho|/|\nabla\rho|_{ref})$) based on the density gradient (greyscale) and pressure (coloured). Note that the image at the top of figure 1(*a*) was for illustration purposes (to show the size of the cone model relative to the tunnel test section), while the cone model was not included in the precursor wind-tunnel simulation.

domain of each DNS box, and the azimuthal direction of each DNS box covered the full circumference of the cone, 2π rad. Here Δx^+ is the streamwise grid spacing along the cone generatrix, $(r\Delta\theta)^+$ and Δz^+ are the azimuthal and wall-normal grid spacing, respectively. The computational grid in the z direction, which stretches close to the wall and is uniform outside the boundary layer, is generated using a hyperbolic tangent function. A similar hyperbolic tangent formula is used to generate an x grid that is very fine near the nose and then uniform in the region downstream. Uniform grids are used in the θ direction. The superscript '+' denotes normalisation by the viscous length z_τ at $x_g = 0.396$ m for all the boxes ($x_g = -0.0005$ m corresponds to the leading edge of the cone), which is the same location where u_τ and δ were extracted. The selection of grid parameters and other aspects of the numerical solution was based on extensive experience with a similar class of flows (Huang *et al.* 2020, 2024). Note that the model for free-stream noise as described by (A1) provides an analytical expression that is valid for all times. Therefore, for a total run length of 0.874 ms, there is no need to repeat a finite-duration time signal.

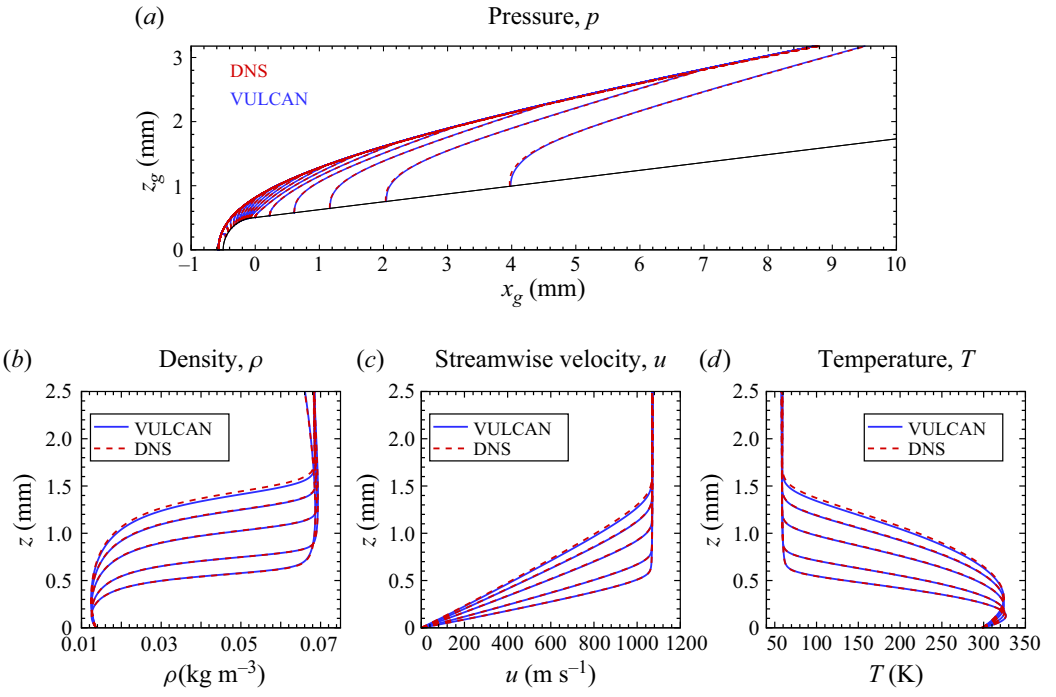

Figure 2. Comparison of the laminar baseflow solutions between DNS (dashed lines) and NASA's VULCAN flow solver (solid lines). The wall-normal profiles were taken at $x_g = 0.05$, 0.1, 0.2, 0.3 and 0.4 m.

Case	$N_x \times N_\theta \times N_r$	x_g (m)	Δx^+	$(r\Delta\theta)^+$	Δz^+	$\Delta t u_\tau/\delta$
Box 1	1536 × 128 × 640	−0.0005–0.03	0.26–4.90	0.0057–8.26	0.005–0.12	6.87×10^{-7}
Box 2	1050 × 128 × 640	0.01–0.11	4.90–6.95	4.30–36.18	0.12–0.55	9.64×10^{-6}
Box 3	1000 × 1024 × 800	0.10–0.23	6.75–6.75	3.92–8.96	0.12–0.25	1.93×10^{-5}
Box 4	1500 × 6000 × 800	0.20–0.40	6.75–6.75	1.31–2.61	0.24–0.46	3.86×10^{-5}
Box 5	1500 × 6000 × 800	0.36–0.56	6.75–6.75	3.35–3.64	0.42–0.64	3.86×10^{-5}

Table 2. Domain size and grid resolution for the DNS runs. Here Δx, $r\Delta\theta$ and Δz represent the grid spacing in the local streamwise, azimuthal and wall-normal directions, respectively. The superscript '+' denotes normalisation by the viscous length z_τ at a reference location of $x_g = 0.396$ m for all the boxes, which is the same location where u_τ and δ were extracted. The total simulation length is 0.874 ms, among which the last 0.2528 ms is used for time-averaged statistics.

2.3. *Assessment of grid resolution and nose radius effects*

To confirm the adequacy of the numerical resolution to capture the high-frequency second-mode waves within the cone boundary layer as well as to assess the possible impact of changing the nose radius from the experimental value of $R_n = 0.05$ mm to $R_n = 0.5$ mm, 2-D axisymmetric DNS involving axisymmetric disturbances at selected frequencies were performed for two nose radii of $R_n = 0.05$ mm and $R_n = 0.5$ mm. In each DNS, small-amplitude, planar, slow acoustic waves with frequencies ranging from 50 kHz to 500 kHz (with an increment of 50 kHz) were imposed at the outer boundary of the DNS domain, which is outside the leading-edge shock of the cone. Specifically, the slow acoustic waves

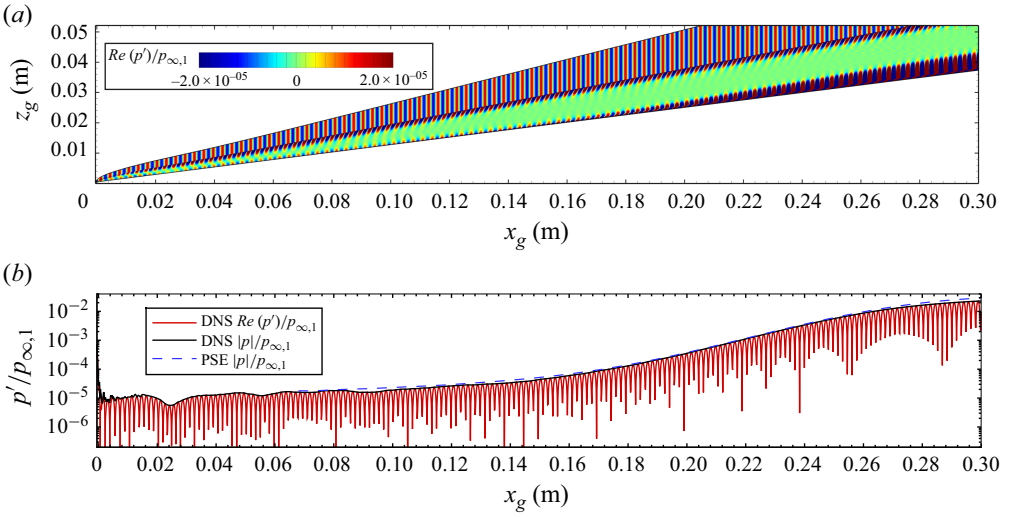

Figure 3. Spatial evolution of pressure fluctuations at $f = 300\,\text{kHz}$ predicted by 2-D axisymmetric DNS of the Mach 8 cone with $R_n = 0.5\,\text{mm}$. (*a*) Contours of $Re(p')$ and (*b*) $|p'|$ and $Re(p')$ at the cone surface, along with the PSE prediction of $|p'|$.

were imposed by using the following equation:

$$\begin{bmatrix} p'_{\infty,1} \\ u'_{\infty,1} \\ T'_{\infty,1} \\ \rho'_{\infty,1} \end{bmatrix} = \begin{bmatrix} 1 \\ -\dfrac{1}{\rho_{\infty,1}c_{1,\infty}} \\ \dfrac{(\gamma-1)T_{\infty,1}}{\gamma p_{\infty,1}} \\ \dfrac{1}{c^2_{\infty,1}} \end{bmatrix} A_p e^{i(k_x x_g - \omega t)} + c.c. \tag{2.1}$$

Here the amplitude A_p was set to $A_p = 3.2 \times 10^{-3}$ Pa and the frequency ω and streamwise wavenumber k_x were related by the dispersion relation $\omega = k_x(U_{\infty,1} - c_{\infty,1})$, where c is the speed of sound. The boundary-layer instabilities excited by the free-stream forcing were subsequently compared at the two nose radii and with those from the stability analysis based on the linear parabolised stability equations (PSE). A similar axisymmetric calculation was conducted by Balakumar *et al.* (2018) for a straight cone with 7° half-angle and several values of the nose bluntness parameter for a free-stream Mach number of 10.

Figure 3 shows the contours of pressure fluctuation due to the free-stream acoustic disturbance at $f = 300\,\text{kHz}$, along with the excited wall-pressure fluctuation amplitude at the cone surface in comparison with the one predicted by the PSE. The free-stream acoustic disturbances pass through the cone shock, get internalised by the boundary layer and excite instabilities inside the boundary layer. The excited instabilities first appeared in the leading-edge region of the cone boundary layer and then started to grow exponentially until saturation was reached near the end of the cone. Figure 4(*a*) shows the N-factors based on wall-pressure fluctuations as computed via the DNS and the linear PSE, respectively, for $R_n = 0.5\,\text{mm}$. A comparison of the DNS results in this case with those for the lower nose radius of $R_n = 0.05\,\text{mm}$ (used in the experiment) is shown in figure 4(*b*). Given that the instability over a sharp cone is dominated by Mack's second-mode waves

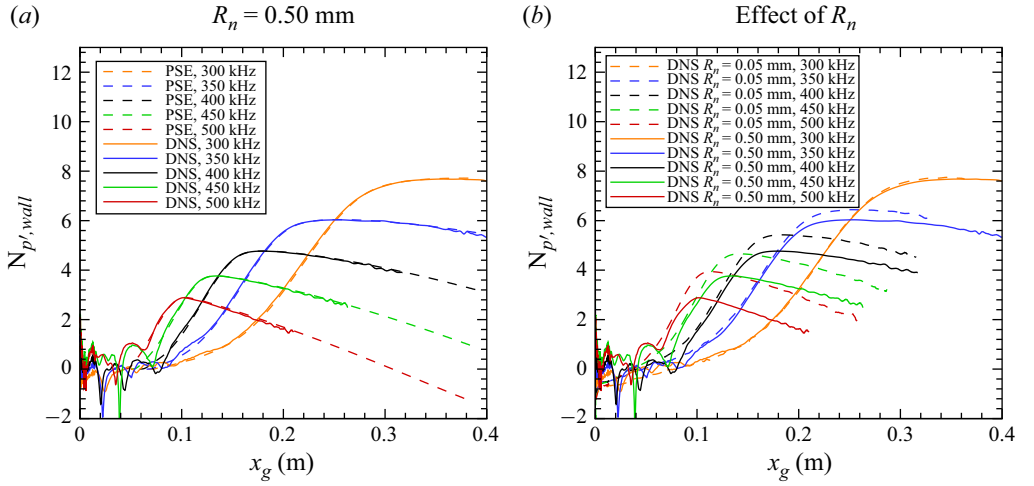

Figure 4. The N-factor curves of the wall pressure predicted by 2-D axisymmetric DNS of Mach 8 cones. (*a*) Comparison with the linear PSE at $R_n = 0.5$ mm; (*b*) comparison between $R_n = 0.05$ mm and 0.5 mm. In each DNS, 10 slow planar acoustic waves are imposed in the free stream with frequency increments of 50 kHz from 50 kHz to 500 kHz.

that are acoustic in nature, they can be well captured by the wall-pressure signal. For both nose radii, the generation of the instability waves inside the boundary layer and their subsequent exponential growth were captured within the DNS. As seen from figure 4(*a*), the N-factors based on the DNS for $R_n = 0.5$ mm are in excellent agreement with those predicted by PSE. The peak N factor increases with frequency, approaching $N = 6$ for $f = 350$ kHz and $N = 7.6$ for $f = 300$ kHz. Although not shown, an equally good comparison with PSE was also obtained for $R_n = 0.05$ mm, indicating the adequacy of the numerical methodology. Figure 4(*b*) indicates moderate differences in the stability characteristics due to the variation of nose radius from $R_n = 0.05$ mm to $R_n = 0.5$ mm. In particular, the N-factor values for $R_n = 0.5$ mm are somewhat lower, consistent with the stabilizing influence of small nose bluntness on the Mack's second-mode waves (Malik *et al.* 1990). The differences between the two cases progressively diminish as the frequency is reduced from $f = 500$ kHz to $f = 300$ kHz, such that the N-factor curves for $f = 300$ kHz nearly overlap with each other for $x_g > 0.1$ m. For $f = 350$ kHz, the difference in peak N-factors for the two nose radii is approximately 0.4.

3. Results

In this section we present the DNS results for BLT at Mach 8 over a 0.56-m-long, 7° half-angle axisymmetric cone with $R_n = 0.5$ mm and $Re_{\infty,1} = 12.2 \times 10^6$ m^{-1}. In the DNS, the BLT was triggered by imposing free-stream acoustic disturbances radiated from the tunnel-nozzle wall, and the details of the tunnel-noise generation are described in Appendix A. Since the DNS domain included the nose tip of the cone with tunnel noise imposed at the free-stream boundary of the computational domain upstream of the bow shock, all stages within transition are taken into account, including the receptivity to free-stream acoustic disturbances, the evolution and breakdown of instability waves and the development of fully turbulent flows. In this section we first visualise the different stages of BLT subject to broadband free-stream acoustic disturbances by using instantaneous DNS data. Next, the DNS results for each stage are discussed and, whenever possible,

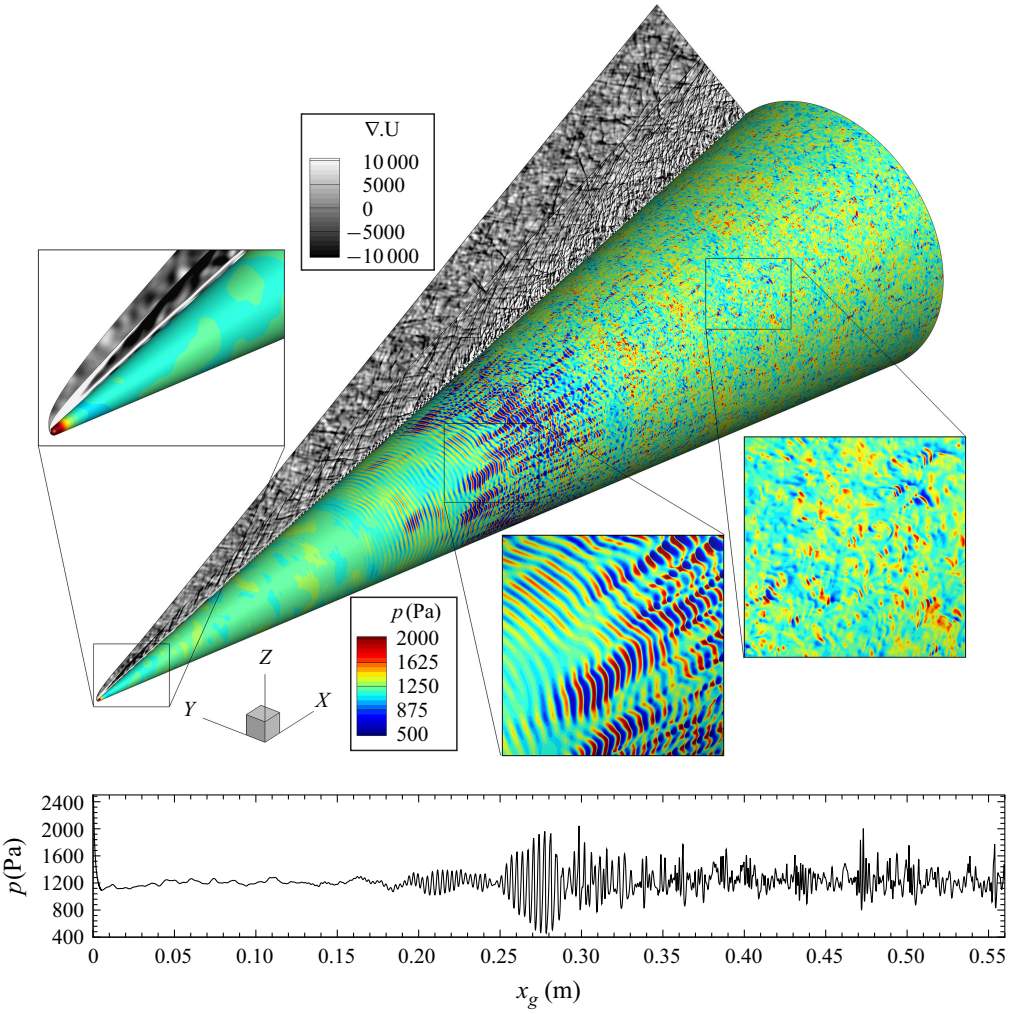

Figure 5. Instantaneous wall pressure (coloured scale) and divergence of the velocity (greyscale) at $t = 0.838$ ms. The plot line was extracted from a row of axial locations along $\phi = 0°$ meridian.

compared with experimental data in the Sandia HWT-8 and other conventional hypersonic wind tunnels.

3.1. *Visualisation of BLT stages*

Figure 5 depicts the contours of instantaneous pressure along the cone surface along with instantaneous velocity contours within a meridional plane at $\phi = 45°$. A line plot of pressure distribution along the $\phi = 0°$ generatrix of the cone is also shown in this figure.

In the upstream region of the cone, where the second-mode waves have not started to amplify as yet, the free-stream acoustic disturbances propagating through the shock have entered the laminar boundary layer, as manifested via the small but non-zero pressure fluctuations measured on the surface. As the second-mode instability grows, azimuthally elongated, roller-like structures appear and undergo small degrees of spanwise meandering. In the breakdown region, the amplitudes of the second-mode wave trains

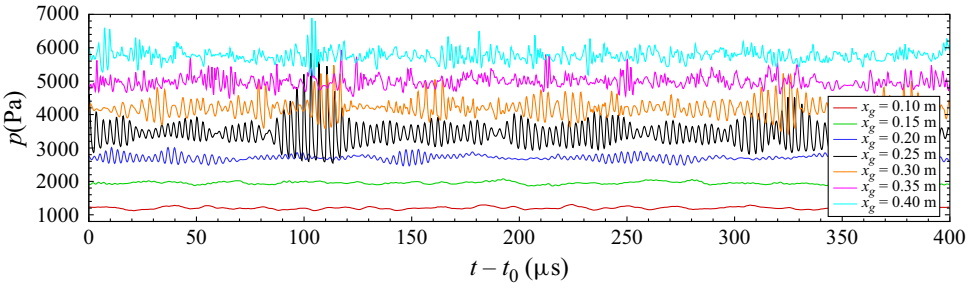

Figure 6. Time trace of wall pressure at different streamwise locations. Starting from $x = 0.15$, the vertical shift is 750 Pa relative to the previous location.

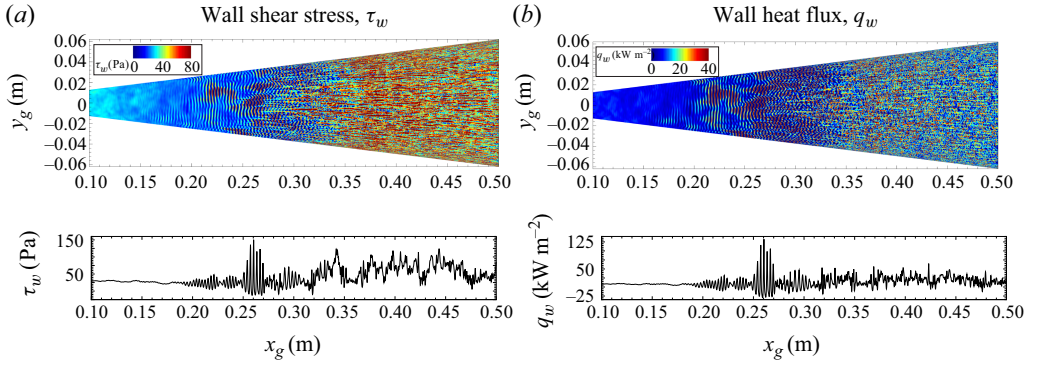

Figure 7. Instantaneous wall shear stress and wall heat flux at $t = 0.8508$ ms. The line plots were extracted from the centre of the contour plots (i.e. along $y_g = 0$).

become strongly modulated in the azimuthal direction, yielding 3-D, azimuthally narrower structures with high amplitude pressure fluctuations. Further downstream, a breakdown of these wave trains leads to a disorganised pattern of small-scale structures. Note that the fluctuation levels of p_w in the initial breakdown region are significantly higher than those in the fully turbulent region, which is consistent with multiple previous findings (Johnson *et al.* 1969; Pate & Brown 1969; Martellucci *et al.* 1973; Cassanto & Rogers 1975; Pate 1978; Casper *et al.* 2016; Kennedy *et al.* 2022). The large amplitude of p'_w is likely caused by repeated intermittent spatial–temporal switching between laminar and turbulent regions. Moreover, the divergence contours also highlight the apparent acoustic radiation emanating from the cone boundary layer in the breakdown and turbulent portion of the cone, which is analogous to the acoustic radiation emanating from the nozzle wall of a conventional wind tunnel.

Figure 6 shows the time trace of wall pressure over a row of axial locations along $\phi = 0°$, where ϕ is the azimuthal angle along the cone surface. Consistent with figure 5, the oscillation amplitude undergoes a significant increase between $x_g = 0.10$ m and $x_g = 0.25$ m, reaching a maximum in the initial breakdown region at $x_g = 0.25$ m, before it decreases at the downstream locations. At $x_g = 0.35$ m, the oscillation signal becomes more chaotic and is free from the wavepackets associated with second-mode waves, indicating the breakdown of second-mode structures and the start of fully turbulent flow.

Figure 7 visualises contours of instantaneous shear stress τ_w and heat flux q_w over the cone surface. For each contour visualisation, a line plot of τ_w and q_w cutting through the centre of the domain (i.e. along $y_g = 0$) was added to emphasise the oscillation amplitudes

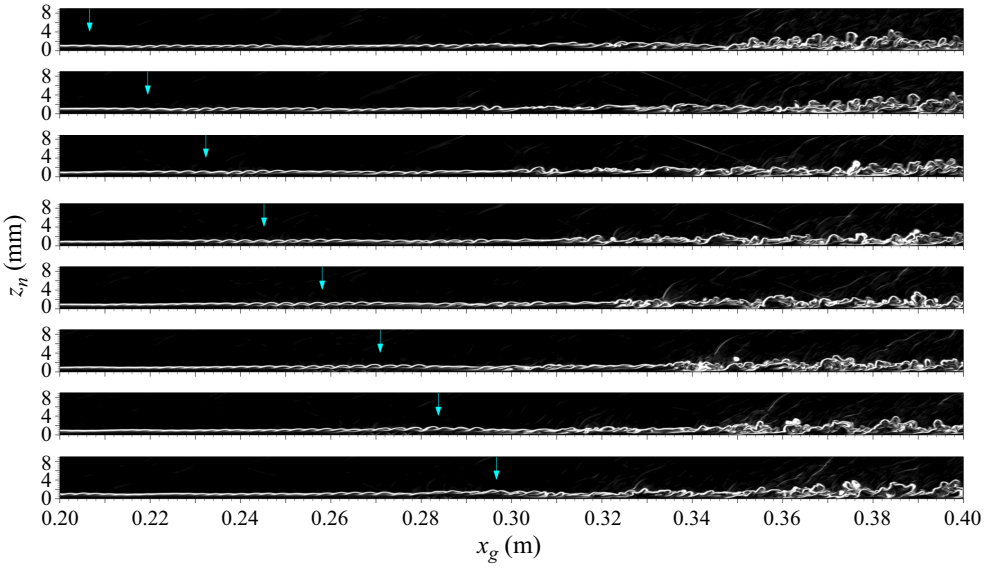

Figure 8. Numerical (synthetic) schlieren based on the density gradient at different times at $\phi = 0°$ and $x_g = [0.20, 0.40]$ m. Here, the frequency of the snapshots is ≈ 78.1 kHz, and the blue arrow denotes the position of a specific wavepacket at different times.

in the pre-transitional, breakdown and fully turbulent regions. For both wall quantities, there is an apparent emergence of quasi-2-D spanwise rollers over $0.10\,\text{m} < x_g < 0.15\,\text{m}$, indicating the dominance of second-mode instability. At $x_g \simeq 0.26\,\text{m}$, the rollers develop strong azimuthal modulation reminiscent of a secondary instability, followed by the intermittent appearance of hot islands or streaks with high levels of wall shear stress and heat-flux fluctuations, indicating the beginning of laminar breakdown. Farther downstream, the hot spots and streaks break down to even smaller structures and the boundary layer becomes fully turbulent. Similar to the wall pressure p_w (figure 5), the fluctuation levels of τ_w and q_w in the initial breakdown region are significantly higher than those in the fully turbulent region.

Figure 8 shows sequenced numerical schlieren images based on the instantaneous density gradient for a typical intermittent disturbance as it forms and breaks down to turbulence over an axial $(x-r)$ plane. Similar to Sandia's experiment (Casper *et al.* 2016), periodic rope-like structures travelling along the wall are clearly seen, and the appearance of such structures is a prominent indicator of second-mode instabilities. The convection speed of the rope structures is estimated to be $U_c \approx 1005\,\text{m}\,\text{s}^{-1}$, which corresponds to approximately 0.93 of $U_{\infty,2}$. At $0.3\,\text{m} \lesssim x_g \lesssim 0.35\,\text{m}$, significant distortion of the rope structures is apparent, leading to the formation of localised turbulence spots that are surrounded by the periodic structures. Farther downstream, even smaller structures emerge in the near-wall region and the laminar breakdown process ensues.

Figure 9 further visualises the instantaneous streamwise velocity at different wall-normal locations within the cone boundary layer. Similar to the wall quantities, the velocity structure consists of quasi-2-D spanwise rollers that undergo spanwise meandering over $0.2\,\text{m} \lesssim x_g \lesssim 0.25\,\text{m}$. Further downstream, the appearance of alternating high-momentum and low-momentum streamwise streaks becomes apparent, and BLT is accompanied by the breakdown of such streamwise streaks into turbulence. The development of streamwise streaks preceding the breakdown to fully turbulent flow is consistent with

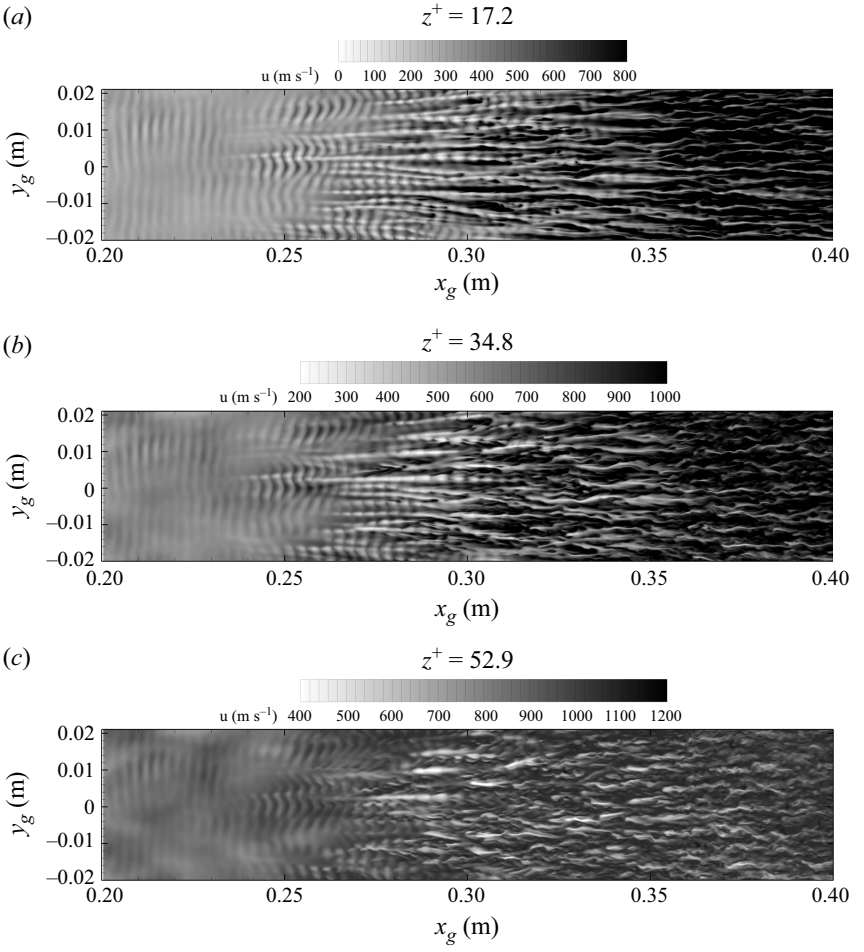

Figure 9. Instantaneous streamwise velocity at different wall-normal locations at $t = 0.838$ ms.

the DNS studies of controlled BLT by Franko & Lele (2013) and Hader & Fasel (2016, 2017, 2018).

3.2. *Amplification of free-stream noise in laminar boundary layer*

In this section the DNS data are analysed to characterise the relationship between the free-stream noise and the fluctuation inside a laminar boundary layer, before instabilities start to grow. The analysis sheds light on how the broadband free-stream noise passes through a shock wave and interacts with a laminar boundary layer over a cone. It also helps quantify the extent of amplification against those by classic theories (Mack 1975; Schopper 1984).

Figure 10(*a*) compares the r.m.s. of pressure fluctuations in the free stream and at the cone surface over the laminar portion of the cone (before instabilities start to grow). As indicated by the blue curve in the figure, the r.m.s. values of the pre-shock pressure fluctuations $(p'_{rms})_{\infty,1}$ are nearly uniform in the axial direction, with $(p'_{rms})_{\infty,1}/(p_{\infty,1}) \simeq 0.04$, which is consistent with the free-stream noise level of 3–5 % for Sandia HWT-8 as reported in Casper *et al.* (2016). The amplitude of pressure fluctuations is increased significantly across the shock in the nose region and approaches a constant value at $x_g \simeq 0.04$ m (or $x_g/R_n \simeq 80$). For $x_g \gtrsim 0.04$ m, no significant difference between $(p'_{rms})_{\infty,2}$ and

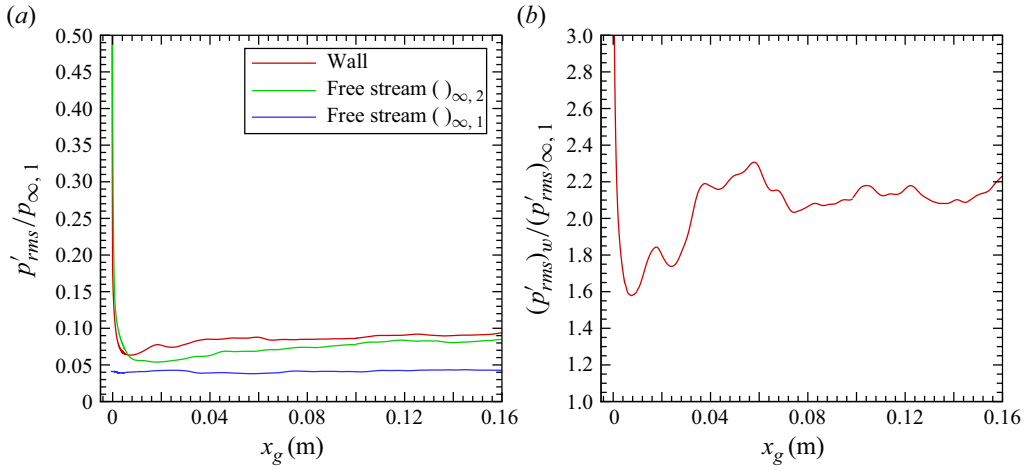

Figure 10. The r.m.s. pressure fluctuations in the free stream (before and after the shock) and at the wall over the laminar portion of the cone.

$(p'_{rms})_w$ is seen, suggesting that most of the amplification of free-stream noise occurred at the shock rather than inside the laminar boundary layer. Figure 10(*b*) further shows that the amplification of the pressure fluctuations at the cone surface relative to the free-stream noise is $(p'_{rms})_w/(p'_{rms})_{\infty,1} \approx 2$, which contradicts the concept of laminar wall-pressure fluctuations being equal to the free-stream tunnel noise (Laderman 1977). Nevertheless, it is consistent with many experimental observations (Beckwith 1975; Kendall 1975; Pate 1980) and the forcing theories by Mack (1975) and Schopper (1984).

Figure 11 compares the normalised power spectral density (PSD) of pressure fluctuations at the wall with the free-stream PSD before and after the bow shock. The PSD results were computed very close to the nose tip at $x_g = 0.01$ m, where the boundary layer remains laminar. The free-stream spectra before and after the shock compare well with each other at all frequencies, indicating that the passage of the free-stream acoustic field through the shock does not modify its frequency content. While the PSD at the wall compares well with those in the free stream at low and mid frequencies, it rolls off faster at high frequencies ($f \gtrsim 100$ kHz). Such a trend is consistent with the theoretical study by Schopper (1984), who found that the high-frequency components of the free-stream noise were low-pass filtered by the upper half of the boundary layer (termed as the caustic layer).

3.3. *Analysis of second-mode amplitudes and transition prediction*

In this section the streamwise evolution of boundary-layer instabilities induced by the tunnel noise is discussed, including the linear and nonlinear evolution of the second-mode waves and their subsequent breakdown to turbulence. In particular, the DNS-predicted second-mode amplitudes and spectra are compared with those measured in the Sandia HWT-8 and several other conventional hypersonic wind tunnels.

Figure 12 shows the frequency PSD and azimuthal wavenumber spectrum (in terms of the azimuthal mode number m) for the wall-pressure fluctuations at different streamwise locations across the pre-transitional and breakdown regions of the cone. For cones in Mach 8 flow at zero angle of attack and with a small nose bluntness of $R_n = 0.5$ mm, the dominant boundary-layer instability is the second-mode instability. It acts like a trapped acoustic wave in the boundary layer, with a dominant frequency that is inversely proportional to the boundary-layer thickness ($f \simeq U_{\infty,2}/2\delta$) (Stetson 1983; Casper 2009;

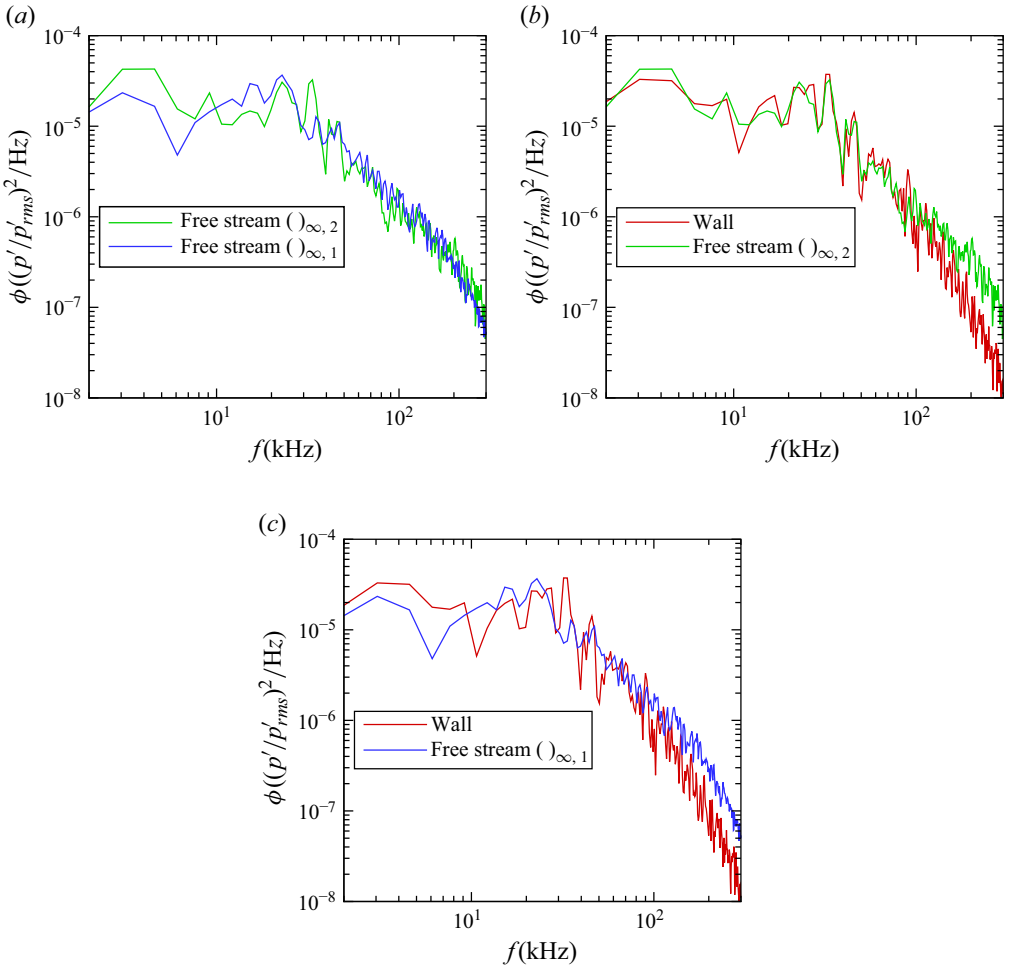

Figure 11. Frequency power spectrum density of pressure fluctuations in the free stream (before and after the shock) and at the wall at $x_g = 0.01$ m.

Casper *et al.* 2016). Starting from $x_g = 0.15$ m, the frequency PSD indicates an apparent spectral hump and higher harmonics. The hump gradually moves to lower frequencies at downstream locations due to the increase in boundary-layer thickness δ, and the peak frequency is consistent with that of the second-mode waves based on stability analysis. At far downstream locations ($x_g \gtrsim 0.35$ m), the second-mode-wave hump in the frequency PSD and its superharmonics are no longer visible, leading to a broadband 'turbulence-like' spectrum. Similar to the frequency PSD, the azimuthal wavenumber spectrum indicates spectral broadening from $x_g \approx 0.15$ m, indicating the emergence of higher azimuthal wavenumbers. As seen from figure 12(*d*), the azimuthal wavenumber spectrum for $x_g \gtrsim 0.35$ m exceeded a threshold value of $\phi((p'/p'_{rms})^2) = 10^{-6}$ for azimuthal wavenumbers up to $m \simeq 800$, indicating the end of structural breakdown and the start of turbulent flow. It may be noted that most of the disturbance energy in the upstream region ($x_g < 0.2$ m) is concentrated in very large azimuthal wavelengths with an azimuthal mode number of $m \lesssim 2$, dropping by an order of magnitude or more for $m > 2$. On the other hand, the nonlinear 3-D structures that manifest in the early phase of the laminar breakdown appear to correspond to $m \geqslant 10$ (figure 12*c*). Further research is needed to

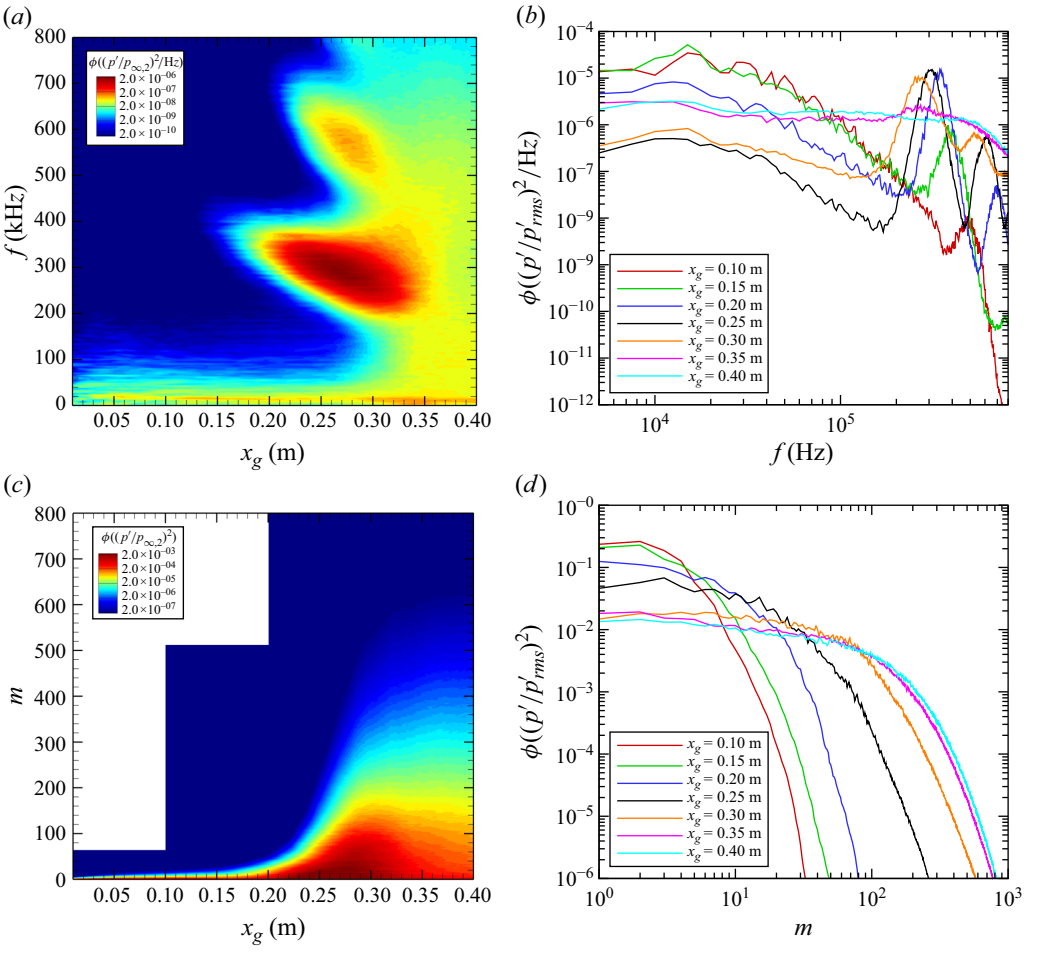

Figure 12. (*a,b*) Frequency PSD and (*c,d*) azimuthal wavenumber spectrum of the wall-pressure fluctuations as a function of streamwise locations x_g.

determine if the higher wavenumber structures are related to secondary instabilities of the rope-like structures associated with finite-amplitude, nearly axisymmetric, second-mode disturbances. Alternatively, they could represent a different breakdown mechanism, such as multiple oblique breakdown induced by the finite bandwidth of low-amplitude, oblique disturbances. The latter mechanism was first revealed in the context of subsonic BLT due to a time harmonic point source (Stemmer *et al.* 1999).

Figure 13 compares the DNS results with the experiment results from the Sandia HWT-8 (Casper 2009; Casper *et al.* 2016; Smith *et al.* 2016), where the BLT was measured over a circular cone with a sharp nose radius of $R_n = 0.05$ mm at several unit Reynolds numbers. In the experiment, axial and spanwise arrays of PCB-132 sensors over the cone surface were used to measure the high-frequency pressure fluctuations associated with the second-mode waves. The PCB-132 sensors, which are difficult to calibrate precisely, can have significant uncertainties for measuring low-amplitude instabilities related to hypersonic BLT (Wason 2019). In particular, a previous study in Sandia HWT-8 (Huang *et al.* 2024) found that the accuracy of PCB-132 sensors at high frequencies can be strongly affected by their finite-sensor diameter d_{probe}. To gauge the influence of the finite-sensor size of

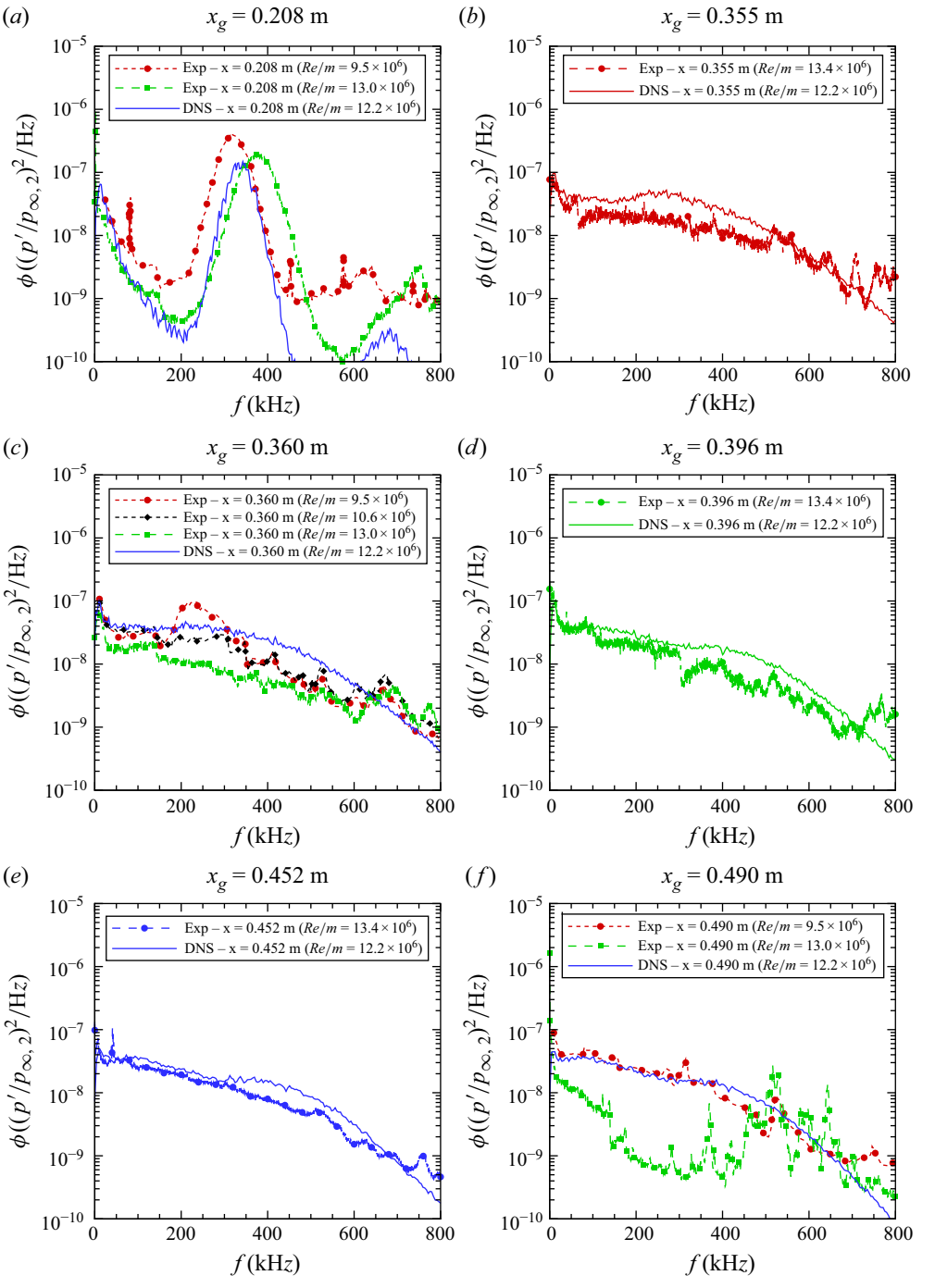

Figure 13. Comparison of wall-pressure fluctuations at multiple axial locations along the cone between DNS and those measured by surface-mounted PCB transducers in Sandia HWT-8 (Casper 2009; Casper *et al.* 2016; Smith *et al.* 2016).

the PCB-132 sensors in the experiment, spatial averaging of the DNS-computed pressure signal over the same circular area of $d_{probe} = 0.98$ mm as the sensing area of the PCB-132 transducer was applied at each measurement location before the comparison with the experiment was performed. A more detailed study of the transducer resolution effect on hypersonic pressure fluctuations was reported by Huang *et al.* (2024). Consistent with figure 12, the PSD of p_w shows a prominent second-mode hump at $x_g = 0.208$ m (see part (*a*) of the figure) that matches well with the measured spectra, with the exception of a somewhat reduced bandwidth in comparison with the experiment. At $x_g \geq 0.355$ m, the prominent second-mode hump is no longer seen in the measured spectrum and has nearly disappeared in the DNS spectrum, indicating the completion of the breakdown of second-mode-wave structures, i.e. transition to turbulence. At all locations (including those in the pre-transitional, breakdown and turbulent regions), the predicted PSD of p_w is consistent with the experimental measurements. In the context of this comparison, it is important to note that the Reynolds and Mach numbers are slightly different. Besides that, the nose radius of the experiment is around 10 times smaller than in our present numerical study as discussed earlier, which can have a non-negligible effect (Stetson 1983). So, we can expect some small mismatches in our results. The influence of the nose radius can also be shown by comparison of the N-factor at $R_n = 0.5$ mm and 0.05 mm (figure 4), wherein both 2-D DNS and PSE indicate a small reduction in the peak amplification of second-mode waves by increasing R_n from 0.05 mm to 0.5 mm. At the measured location of $x_g \approx 0.275$ m where the r.m.s. pressure fluctuations on the surface peaks, the N-factor for the 0.05 mm nose tip is 7.14, while the N-factor value at this location is 7.00 for the 0.5 mm nose tip cone. The small change in the peak N-factor of dominant modes of the second-mode instability effectively represents a somewhat weaker (and slightly delayed) growth of instabilities in the DNS, due to a larger value of R_n, or equivalently, a larger nose radius Reynolds number Re_n in comparison with the experiment. The nose radius can also influence the receptivity process. Based on the limited available information of receptivity to planar acoustic disturbances (Balakumar & Kegerise 2011; Kara *et al.* 2011) and the § 2.3 computations, second-mode receptivity tends to decrease with increasing nose radius Reynolds number, Re_n. Combined with the small stabilizing influence of Re_n on the linear growth factors at $R_n = 0.5$ mm, this would imply a somewhat delayed onset of transition in the DNS relative to the experiment. While this trend is consistent with the nonlinear saturation characteristics of second-mode pressure fluctuations, as will be shown in figure 14(*b*), definitive conclusions regarding the effects of the larger nose radius in the DNS are precluded by two factors: limited available information on the receptivity of second-mode disturbances under broadband forcing and the effect of R_n on subdominant disturbances that might play a role during the nonlinear stage of transition. Additional DNS for smaller nose radii would be useful to further elucidate the effects of nose tip radius on transition, especially at the small nose tip radii of interest, where second-mode growth clearly dominates the overall transition process.

Figure 14 compares the maximum and initial second-mode amplitudes predicted by the current DNS against sharp-cone measurements from multiple conventional wind tunnels (Marineau *et al.* 2019). Here, the maximum or breakdown amplitude A_{max} is measured by the maximum r.m.s. pressure fluctuations on the surface of the cone, and the initial amplitude A_o is estimated from A_{max} and the N-factor value from the linear PSE (figure 4*a*) following the procedure outlined in Marineau *et al.* (2019). For both DNS and experiment cases, the maximum breakdown amplitude lies between 20 % and 35 % relative to the boundary-layer edge mean pressure $p_{\infty,2}$, and the DNS-predicted maximum amplitude is slightly higher than most of the experimental results. However, excellent

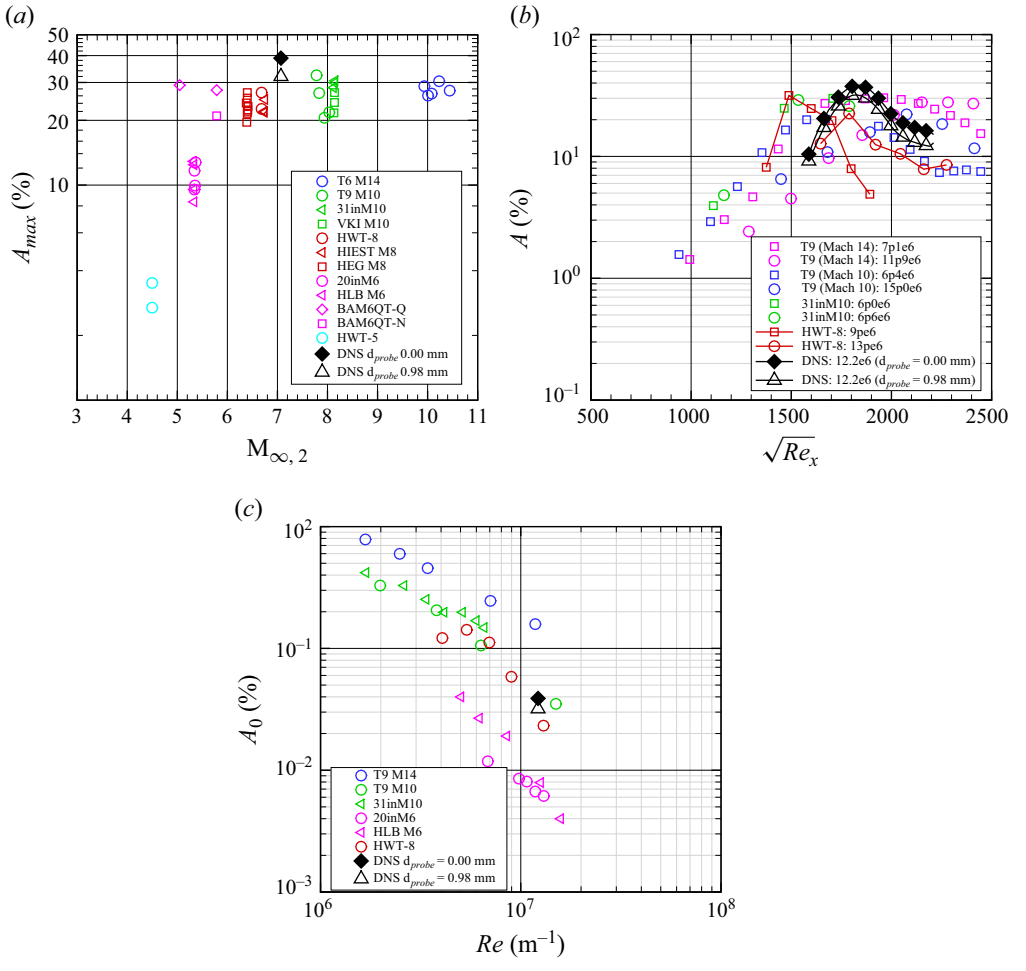

Figure 14. Amplitudes of the second mode (measured by $p'_{w,rms}/p_{\infty,2}$) in comparison with sharp-cone measurements in multiple conventional hypersonic wind tunnels as reported in Marineau *et al.* (2019).

agreement between the DNS and experiments is achieved after accounting for the finite-size effect in the DNS by spatially averaging the computed pressure signal with the same sensor area of the PCB-132 sensor. A similar approach to account for the finite-sensor effect has been applied in Huang *et al.* (2024). Similarly, very good agreement is achieved for the initial amplitude A_o.

Figure 15 compares the DNS-predicted transition location against Pate's empirical correlation (Pate 1978). Here, the transition location was defined as the streamwise location where the wall-pressure fluctuations reached the peak value. The same definition was used by Casper (2009) for her experimental study in Sandia HWT-8. The DNS predicted a transition location of $x_{tr} = 0.275$ m at $Re/m = 12.2 \times 10^6$, which compares very well with Pate's theory and is also consistent with the locations of experimentally measured peak pressure fluctuations as reported in Casper (2009) and Casper *et al.* (2016). The excellent comparison of DNS against established correlations and experiments confirms the efficacy of the tunnel-noise model used to trigger transition in the DNS. Given that Pate's correlation was derived for estimating the transition location on sharp

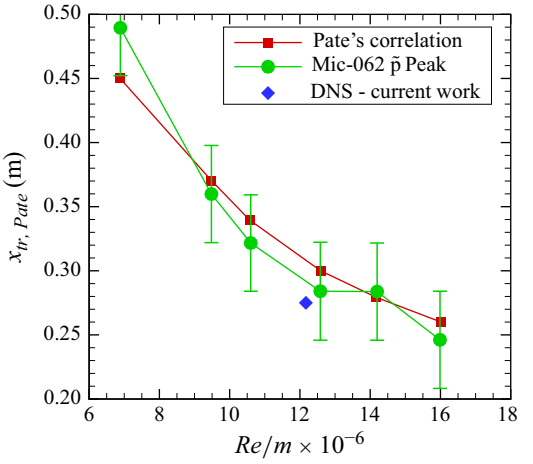

Figure 15. Comparison of the transition location between DNS and the empirical correlation of Pate (1978).

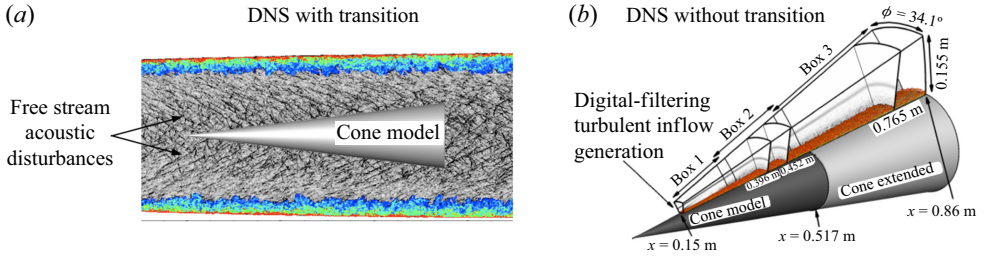

Figure 16. Comparison of the domain and set-up between the current DNS with tunnel-noise-induced BLT (left) and that without BLT by Huang *et al.* (2024) with a nominal Mach number of 8 and $(Re_{unit})_{\infty,1} = 12.8 \times 10^6$ (right).

cones at zero angle of attack, the good comparison between the DNS and Pate's theory also confirms that the influence on stability characteristics due to a nose bluntness of $R_n = 0.5$ mm was small.

3.4. *Turbulent flow development*

Having examined the crucial stages of second-mode induced BLT in § 3.3, the current section characterises turbulent flow development in the post-transitional region of the boundary layer. In addition to natural transition induced by tunnel-like free-stream disturbances, one additional DNS was conducted wherein BLT was bypassed and turbulence was forced by an artificial turbulence generation method at the domain inlet located at $x_g = 0.15$ m. The details of the turbulent cone DNS were documented in Huang *et al.* (2024). A comparison of the domain and set-up between the DNS with and without BLT is shown in figure 16. The two DNS runs were compared to investigate and determine the effect of upstream transition mechanisms on the turbulent boundary layer developed downstream, and such a comparison should provide critical information on whether certain significant flow characteristics are linked to either the transitional region and/or the inflow conditions.

To confirm fully turbulent flow toward the end of the DNS domain, figure 17 compares the evolution of the Stanton number C_h against those of the van Driest II theory

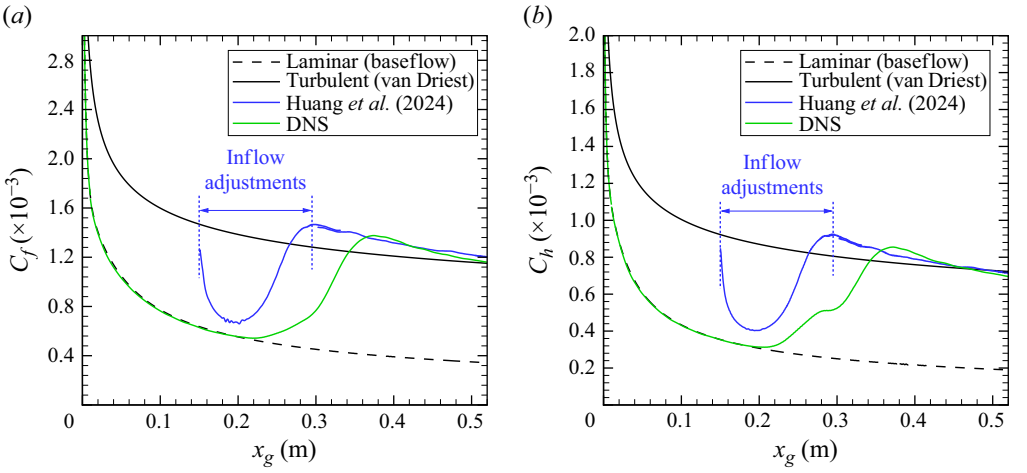

Figure 17. Streamwise evolution of (*a*) skin-friction coefficient and (*b*) Stanton number in comparison with those of the laminar baseflow, the van Driest II theory and the turbulent cone DNS with artificial inflow turbulence generation by Huang *et al.* (2024).

(Driest 1956*b*) and the turbulent cone DNS of Huang *et al.* (2024). Here, the skin-friction coefficient and Stanton number are defined as

$$C_f = \frac{\tau_w}{0.5\rho_{\infty,2}U_{\infty,2}^2}, \qquad C_h = \frac{q_w}{\rho_{\infty,2}U_{\infty,2}C_p(T_r - T_w)}. \tag{3.1}$$

In deriving the theoretical turbulent-skin-friction value of a cone, a simple cone rule based on the von Karman momentum integral (White & Corfield 2006) was used, i.e.

$$C_{f,Cone} = C_{f,Flat\,Plate} \times G, \tag{3.2}$$

where $1.087 < G = (2+m)^{m/(m+1)} < 1.176$ (or $1/8 < m < 1/4$). In the present work, the value of m was chosen to be approximately $1/7$ with $G = 1.1$. The theoretical turbulent Stanton number was further calculated according to the well-known Reynolds analogy as

$$C_{h,cone} = \frac{C_{f,cone}}{2Pr^{2/3}}. \tag{3.3}$$

Both C_f and C_h remained laminar baseflow values until $x_g \approx 0.2$ m, which approximately coincides with the peak location of the modal amplitude of the second-mode waves shown in figure 12(*b*). At $x_g \approx 0.2$ m, the skin friction and Stanton number rapidly departed from the laminar values and approached the turbulent values predicted by the van Driest II theory. We observe that C_h shows an intermediate plateau during transition near $x_g \simeq 0.3$ m. We have confirmed that the emergence of this plateau is not caused by the limited duration of the DNS data. However, further work is necessary to clarify the mechanism for the appearance of the plateau. Both C_f and C_h overshoot their turbulent predictions by the van Driest II theory during transition and reached a peak value at $x_g \simeq 0.35$ m that is more than three times greater than the laminar baseflow value. Similar overshoot in C_f and C_h was found by Franko & Lele (2013) for BLT over a Mach 6 flat-plate boundary layer. Note that C_f and C_h predicted by Huang *et al.* (2024) underwent a similar overshoot over the

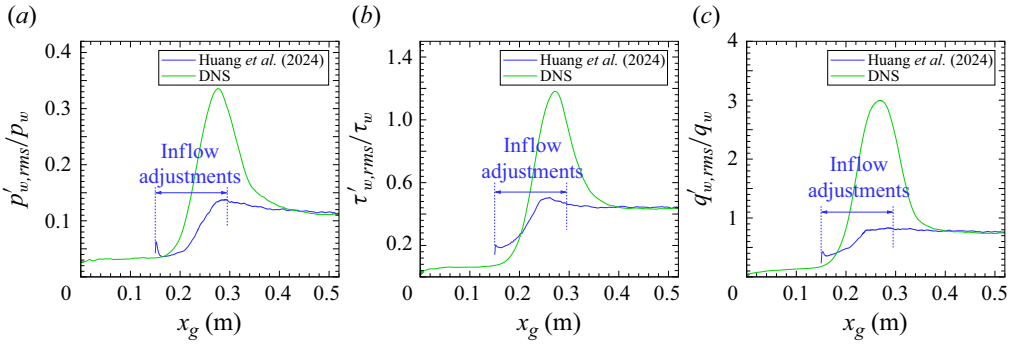

Figure 18. Comparison of (*a*) r.m.s. wall pressure, (*b*) r.m.s. skin friction and (*c*) r.m.s. wall heat flux against those of the turbulent cone DNS by Huang *et al.* (2024).

turbulent predictions. Towards the end of the domain ($x_g \gtrsim 0.40$ m), C_f and C_h showed excellent comparisons against those of the van Driest II theory and the turbulent DNS by Huang *et al.* (2024).

Figure 18 shows the r.m.s. of wall pressure, wall skin-friction and wall heat-flux fluctuations normalised by their local mean values as a function of the streamwise coordinate, and the turbulent cone results from Huang *et al.* (2024) are included for comparison. Due to the amplification of free-stream noise by the shock and cone laminar boundary layer, the r.m.s. of the pressure, skin-friction and heat-flux fluctuations maintained a small but non-zero value of 3.5 %, 8.2 % and 17.5 %, respectively, in the upstream laminar region. Starting from $x_g \simeq 0.2$ m, the laminar boundary layer is significantly modulated by the second-mode structures and all the fluctuating wall quantities undergo a rapid increase in amplitude, reaching peak values of 33.5 %, 118.1 % and 300.0 %, respectively, relative to the mean in the initial breakdown region at $x_g \simeq 0.27$ m. In the post-breakdown and turbulent region, the fluctuating wall quantities are nearly uniform, approximately equal to 11.5 %, 42.1 % and 69.5 % respectively. The significantly larger amplitudes of the fluctuating wall quantities in the breakdown region relative to those in the laminar or fully turbulent regions is in agreement with the literature (Johnson *et al.* 1969; Pate & Brown 1969; Martellucci *et al.* 1973; Cassanto & Rogers 1975; Pate 1978; Casper *et al.* 2016; Kennedy *et al.* 2022) as well as the visualisations in figures 5 and 7. The overshoot in wall quantities was likely caused by repeated intermittent spatial–temporal switching between laminar and turbulent regions. Note that while the results of Huang *et al.* (2024) wherein BLT was bypassed predicted similar overshoots in mean values as the current DNS with BLT, it underpredicted the transitional peak of all the fluctuating wall quantities by at least a factor of 2. Such a trend suggests that BLT, and laminar breakdown in particular, needs to be accurately simulated or modelled in order to capture the overshoot in fluctuating wall quantities. In the fully turbulent region, both DNS with and without BLT compare well for all the wall quantities, indicating minimal impact of upstream transition mechanisms on the development of the turbulent boundary layer in the downstream most portion of the cone. Recall that the overshoot of the skin-friction coefficient (C_f) and Stanton number (C_h) occurred at $x_g \approx 0.38$ m, which lags the overshoot in fluctuating wall quantities (τ'_w, q'_w) at $x_g \approx 0.3$ m, potentially indicating the finite length required for the mean flow to adjust to the overshoot in fluctuations.

Figure 19 plots the mean streamwise velocity transformation based on Driest (1956*a*) at various streamwise locations across the transitional and turbulent portions of the cone.

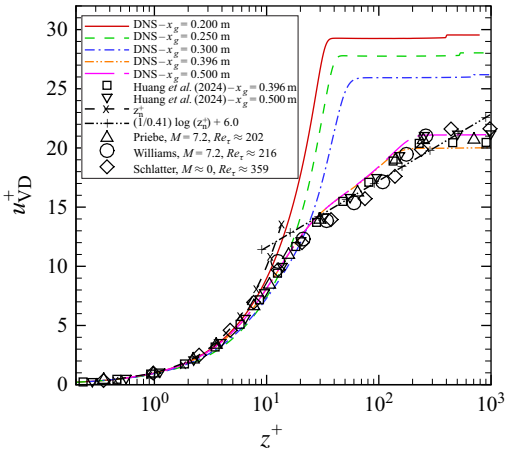

Figure 19. Comparison of the van Driest transformed mean streamwise velocity against those of the turbulent cone DNS by Huang *et al.* (2024) and other flat-plate experimental and DNS data. Symbols: △, Priebe & Martin (2011); ◯, Williams *et al.* (2018); ♢, Schlatter & Örlü (2010).

The van Driest (VD) transformation is defined as

$$u_{\mathrm{VD}}^+ = \int_0^{\overline{u}^+} (\overline{\rho}/\overline{\rho}_w)^{1/2} d\overline{u}^+, \tag{3.4}$$

and the boundary-layer profiles for the van Driest transformation are plotted in inner units as

$$z^+ = \frac{\overline{\rho}_w (\tau_w/\overline{\rho}_w)^{1/2} z}{\overline{\mu}_w}. \tag{3.5}$$

As the flow developed from laminar to turbulent flow, the mean profile evolved from that of a laminar boundary layer to that of a turbulent boundary layer. Immediately downstream of the transition location at $x_g \simeq 0.3$ m, the mean profile matched closer to the expected turbulent streamwise velocity profile than those in the pre-transitional region but still did not match well in the log-law region. At $x_g \simeq 0.396$ m and farther downstream, the profile indicates a smaller deviation from the reference streamwise velocity profile than the pre-transitional profile in both the viscous sublayer and the low-law region, confirming the fully turbulent nature of the flow beyond $x_g = 0.396$ m. A similar trend was seen for the Reynolds stresses (figure 20) and turbulent heat flux (figure 21), which compared well with those of the turbulent DNS by Huang *et al.* (2024) and other DNS studies of high-speed turbulent boundary layers towards the end of the domain ($x_g \gtrsim 0.396$ m).

The temperature–velocity correlation coefficient ($R_{u''T''}$) and turbulent Prandtl number (Pr_t) are defined as

$$R_{u''T''} = \frac{\widetilde{u''T''}}{\sqrt{\widetilde{T''^2}}\sqrt{\widetilde{u''^2}}}, \qquad Pr_t = \frac{[\overline{\rho u'' w''}](\partial \tilde{T}/\partial z)}{[\overline{\rho T'' w''}](\partial \tilde{u}/\partial z)}. \tag{3.6}$$

Figure 22 further shows that the temperature–velocity correlation coefficient ($R_{u''T''}$) and turbulent Prandtl number (Pr_t) follow the expected relationship between velocity and temperature for high-speed turbulent boundary layers at $x_g \gtrsim 0.396$ m.

Figures 23(a) and 23(b) compare the frequency PSD and the azimuthal wavenumber spectrum, respectively, between the present DNS and those by Huang *et al.* (2024) at

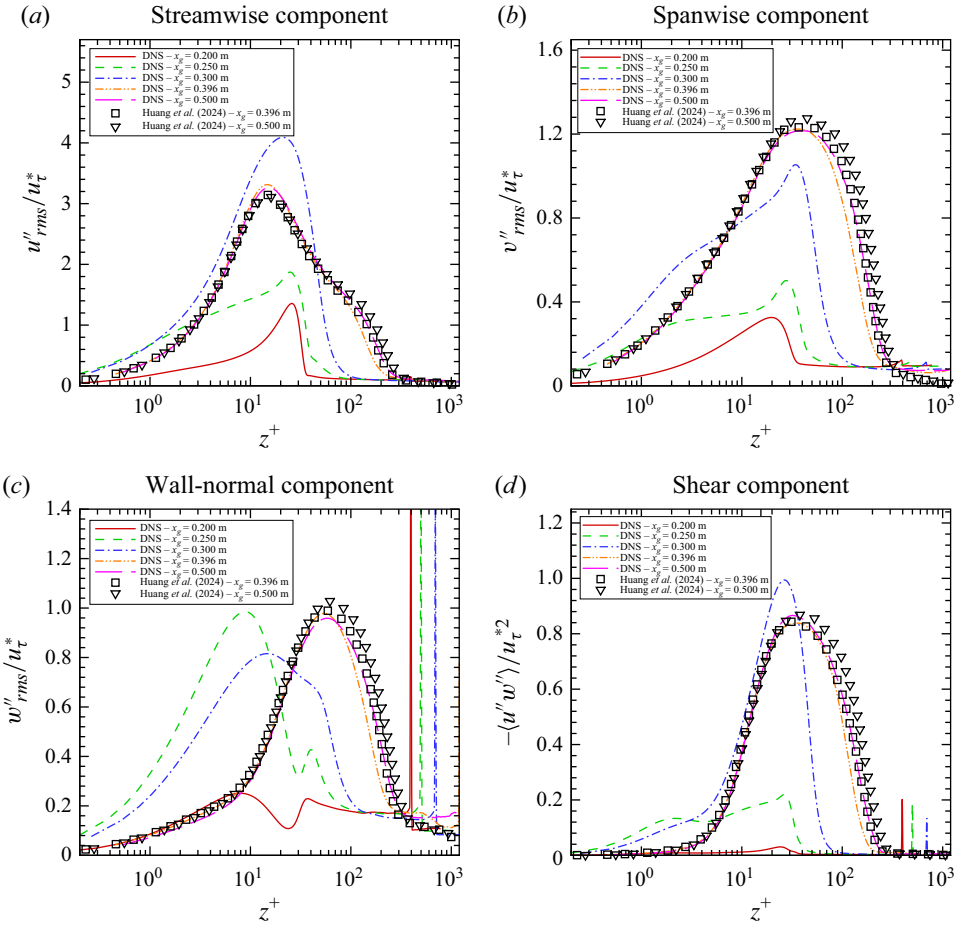

Figure 20. Comparison of density-weighted turbulence intensities with those from the turbulent cone DNS by Huang *et al.* (2024). $u^*_\tau = (\overline{\rho}_w/\overline{\rho})^{1/2}u_\tau$ is the density-weighted velocity scale.

two axial locations in the post-transitional region. The azimuthal wavenumber spectrum shows excellent agreement at all azimuthal wavenumbers for the DNS cases with and without BLT. Similarly, a good comparison is observed for the frequency PSD at mid and high frequencies. However, there exist appreciable differences in the PSD at the lowest frequencies ($f \lesssim 50$ kHz), where the DNS that included the second-mode-induced transition process predicts higher amplitudes in the lower-frequency range and, as a result, shows significantly improved comparison with the measured spectra based on surface-mounted PCB transducers. These findings suggest the persistence of the low-frequency structures up to at least $x_g = 0.54$ m. Such low-frequency structures were also streamwise elongated according to Taylor's hypothesis, which left a footprint on the lowest-frequency contents of the wall-pressure signal but had a negligible impact on single-point turbulence statistics like the Reynolds stresses and turbulent heat flux.

Figure 24 visualises the coherent structures in the near-wall and outer layer of the cone boundary layer for current DNS datasets in comparison with those of Huang *et al.* (2024). Both DNS results indicate near-wall streaks at $z^* \approx 15$ as well as alternating long streamwise structures of uniform low- and high-speed fluid with length at least 10δ in the outer layer of the boundary layer. There is an apparent similarity in large-scale coherent

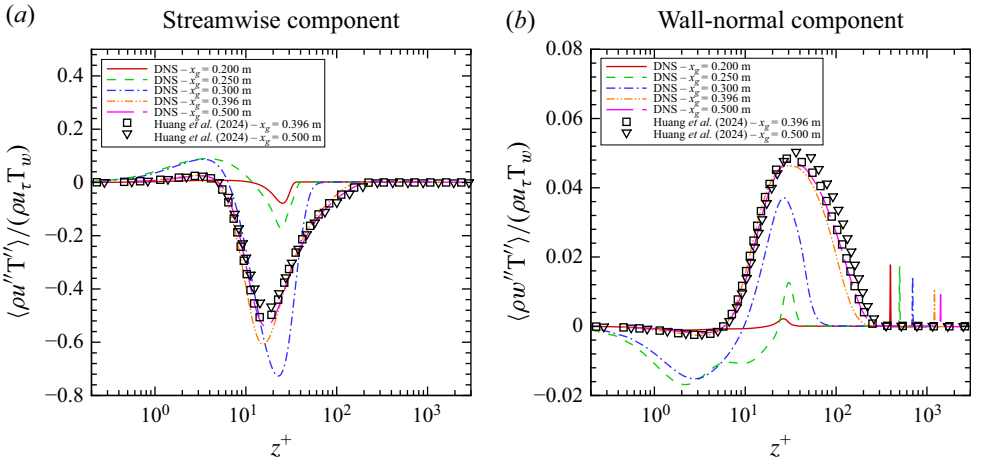

Figure 21. Comparison of (*a*) streamwise and (*b*) wall-normal components of the turbulent heat flux against those of the turbulent cone DNS by Huang *et al.* (2024).

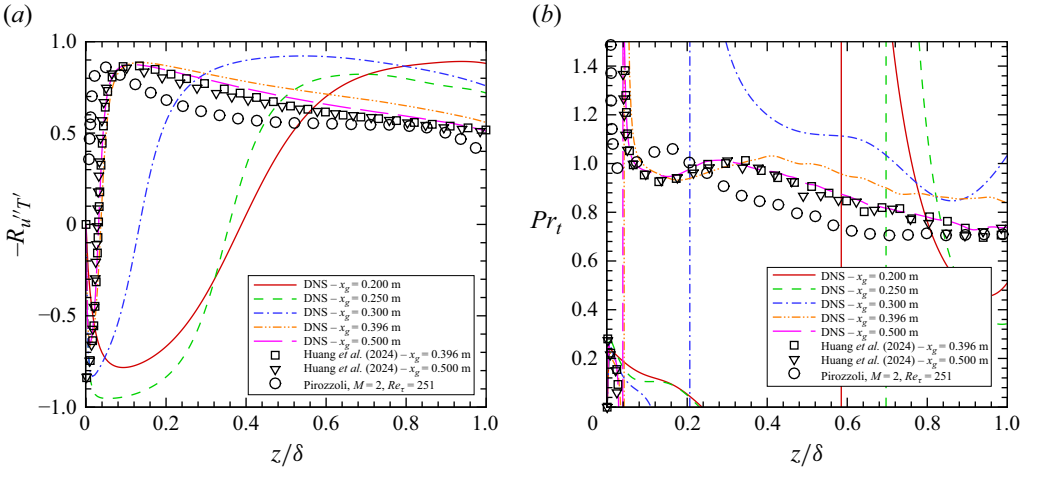

Figure 22. Comparison of (*a*) temperature–velocity correlation coefficient $R_{u''T''}$ and (*b*) turbulent Prandtl number Pr_t against those of the turbulent cone DNS by Huang *et al.* (2024) and the flat-plate DNS by Pirozzoli & Bernardini (2011) at $M = 2$ and $Re_\tau = 251$.

structures between the DNS cases with and without BLT, and these structures were also similar to those identified in the studies for flat-plate turbulent boundary layers (Duan *et al.* 2010, 2011; Huang *et al.* 2022), suggesting that the flow structures in the fully turbulent region do not heavily depend on the cause of turbulence. We also note that the streamwise elongated structures in the logarithmic and outer regions of the boundary layer appear to be more organised and larger in size for the DNS case with BLT, which may have left a stronger footprint on the wall at the lowest frequencies as suggested by figure 23(*a*).

4. Conclusion

In this work, we presented DNS of the natural transition process over a 7° half-angle cone with a small nose radius of $R_n = 0.5$ mm in a Mach 8 free-stream at a unit Reynolds number of 12.2×10^6 m^{-1}. The generation of boundary-layer instabilities was triggered by

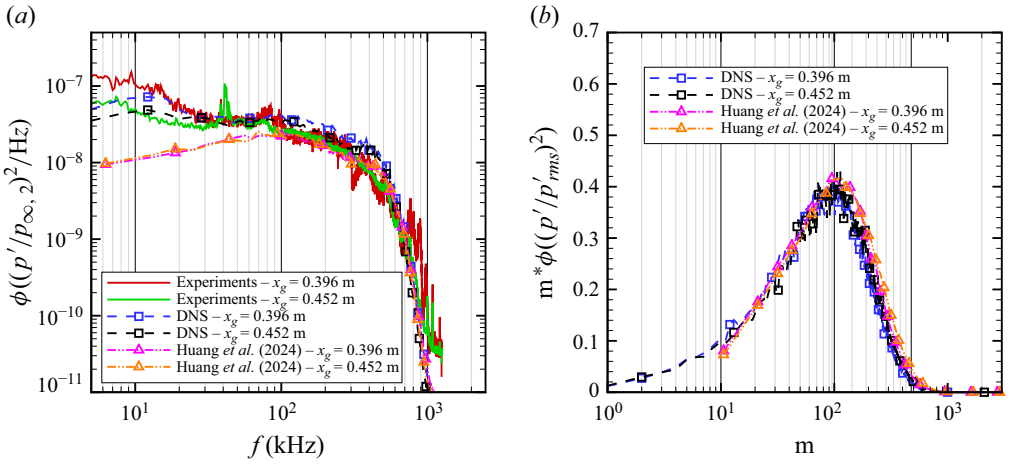

Figure 23. Comparison of (*a*) frequency PSD and (*b*) azimuthal wavenumber spectrum of the wall-pressure fluctuations against those of Huang *et al.* (2024). The DNS-predicted spectrum in (*a*) was spatially averaged over the surface grid points within a diameter of 0.98 mm to match the sensing area of the PCB piezotronics.

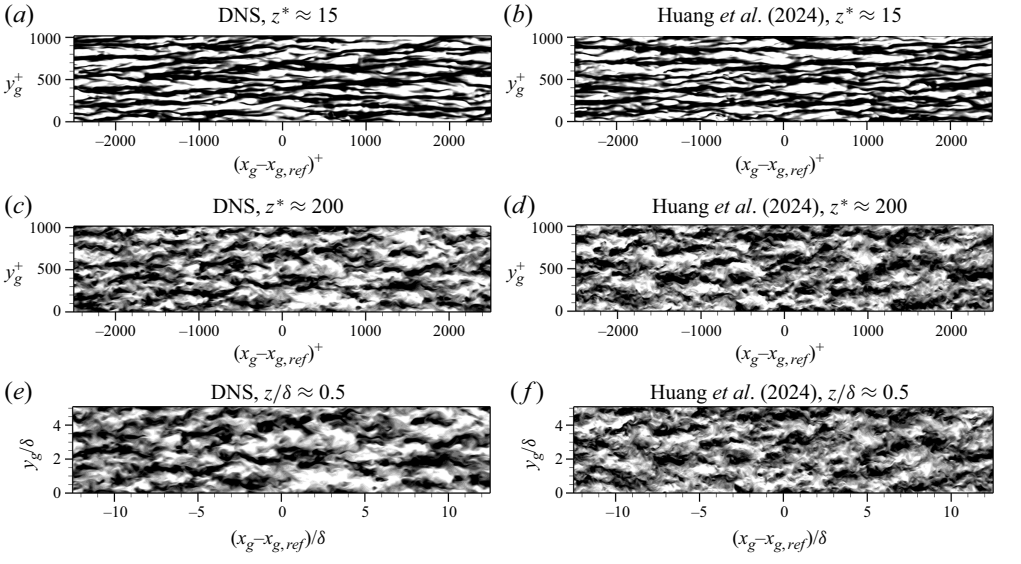

Figure 24. Visualisation of the streamwise velocity fluctuations at $x_{ref} \approx 0.53$ m for the current DNS with BLT (left column) against those of the DNS without BLT by Huang *et al.* (2024) (right column). A streamwise range of δ centred at the downstream turbulent portion of the computation domain was selected for each case, where δ is the local boundary-layer thickness at the reference location $x_{g,ref} \approx 0.53$ m. The heights are selected at (*a,b*) $z^* \approx 15$, (*c,d*) $z^* \approx 200$ and (*e,f*) $z/\delta \approx 0.5$. Flood contour levels are shown for $-2 \leqslant \sqrt{\rho}u''/\sqrt{\tau_w} \leqslant 2$ from dark to light shades. Inner scales are used in (*a,b*) and outer scales in (*c,d,e,f*).

tunnel-like broadband free-stream acoustic disturbances radiated from the axisymmetric nozzle wall of the Sandia HWT-8. All the stages during transition to turbulence due to the tunnel noise were studied, including the passage of broadband free-stream noise through the shock wave, the generation of Mack's second-mode waves within the laminar cone boundary layer through receptivity mechanisms, the nonlinear growth of those instabilities to saturation, their laminar breakdown to turbulence and the fully turbulent flow. Before the

second-mode instabilities began to amplify, the interaction of free-stream noise with the shock and the laminar cone boundary layer led to amplification in disturbance amplitude and non-zero wall-pressure fluctuations at the cone surface. While the passage of the free-stream acoustic field through the cone shock wave did not lead to a qualitative change in the spectral behaviour, the high-frequency components of the free-stream noise were low-pass filtered within the laminar boundary layer. The DNS successfully predicted second-mode instabilities as rope-like structures travelling parallel to the wall, which were similar to the schlieren visualisations in the Sandia facility. The frequency spectrum of pressure fluctuations over the cone surface exhibited a spectral hump in the range of the second-mode waves and their higher harmonics prior to the onset of the laminar breakdown. The breakdown amplitude A_{max} of second-mode waves compared well with the sharp-cone measurements from multiple conventional wind tunnels as reported by Marineau *et al.* (2019). The computed spectra of transitional and turbulent pressure fluctuations at the cone surface were in excellent agreement with the measured data in the Sandia facility, after accounting for the finite size of the pressure transducers used in the experiment. The transition location predicted by the DNS compared well with Pate's correlation and was also consistent with the location of peak measured pressure fluctuations in the Sandia HWT-8. Near the end of transition, the computed skin friction and Stanton number distributions exhibited overshoots relative to the fully turbulent predictions by the van Driest II theory. The associated fluctuations in these wall quantities were also larger than those in the fully turbulent regions of the computed flow field. The comparison between DNS predictions of fully turbulent flow with and without natural BLT confirmed the existence of fully turbulent flow near the end of the cone in the case with BLT, such that the mean boundary-layer profiles, Reynolds stresses and turbulent heat flux were nominally free of upstream history effects. While not comprehensive, high-frequency turbulent fluctuations in the fully turbulent region do not depend heavily on the cause of turbulence. However, the breakdown of the second-mode structures may leave a long-lasting footprint on the lowest-frequency contents of the wall-pressure fluctuations in the turbulent portion of the cone, which could explain the closer agreement between the DNS with BLT and the experimental measurements in the low-frequency bandwidth of wall-pressure fluctuations.

The physical realism and accuracy of the computed flow fields confirmed the adequacy of the numerical procedure for imposing a 'tunnel-noise' model to mimic the disturbance environment in a conventional hypersonic wind tunnel. It therefore established the foundation for a 'virtual' testing of the hypersonic BLT in a noisy digital wind tunnel. While the present study has provided valuable insight into the onset of 3-D perturbations that are likely to trigger the onset of transition, significant future work is necessary to distill the precise physical mechanism involved.

Funding. The Ohio State University (OSU) acknowledges funding support from Sandia National Laboratories. Partial support for the OSU group was also provided by the Office of Naval Research (under grants N00014-17-1-2347 and N00014-23-1-2456, managed by Dr. Eric Marineau). M.M.C was supported by the Hypersonic Technology Project (HTP) under the NASA Aeronautics Research Mission Directorate (ARMD). P.P. was partially supported by the ONR under grants N00014-20-1-2261 and N00014-23-1-2456 and by the HTP under the NASA ARMD. Computational resources were provided by the DoD High Performance Computing Modernisation Program and the Innovative and the Novel Computational Impact on Theory and Experiment (INCITE) program. Sandia National Laboratories is a multimission laboratory managed and operated by National Technology and Engineering Solutions of Sandia, LLC., a wholly owned subsidiary of Honeywell International, Inc., for the U.S. Department of Energy's National Nuclear Security Administration under contract DE-NA0003525. The views and conclusions contained herein are those of the authors and should not be interpreted as necessarily representing the official policies or endorsements, either expressed or implied, of the funding agencies or the U.S. Government.

Declaration of interests. The authors report no conflict of interest.

Appendix A. 'Tunnel-like' acoustic disturbance generation

This appendix outlines the procedure for generating tunnel-like free-stream acoustic disturbances, building upon the discussion originally presented in Liu *et al.* (2022). The tunnel-noise model is formulated using an ansatz of slow plane acoustic waves and the model parameters are calibrated via a precursor DNS that simulates the acoustic field radiated from the turbulent nozzle-wall boundary layer of a hypersonic wind tunnel.

A.1 *Formulation of free-stream acoustic disturbance model*

The acoustic perturbations in the free stream outside of the turbulent boundary layer are represented as the superposition of a large number of plane-wave components:

$$\begin{bmatrix} p'_{\infty,1} \\ \rho'_{\infty,1} \\ u'_{\infty,1} \\ v'_{\infty,1} \\ w'_{\infty,1} \\ T'_{\infty,1} \end{bmatrix} = \sum_{j=1}^{N} \begin{bmatrix} 1 \\ \dfrac{1}{\bar{c}^2_{\infty,1}} \\ \dfrac{1}{\bar{\rho}_{\infty,1}\bar{c}_{1,\infty}} \left(\dfrac{k_{x,j}}{\|\mathbf{k}_j\|} \right) \\ \dfrac{1}{\bar{\rho}_{\infty,1}\bar{c}_{1,\infty}} \left(\dfrac{k_{y,j}}{\|\mathbf{k}_j\|} \right) \\ \dfrac{1}{\bar{\rho}_{\infty,1}\bar{c}_{1,\infty}} \left(\dfrac{k_{z,j}}{\|\mathbf{k}_j\|} \right) \\ \dfrac{(\gamma-1)\overline{T}_{\infty,1}}{\gamma \overline{p}_{\infty,1}} \end{bmatrix} \hat{p}_j(\mathbf{k}_j, \omega_j) e^{i(\mathbf{k}_j \cdot \mathbf{x} - \omega_j t + \phi_j)} + c.c. \tag{A1}$$

Here, $\mathbf{x} = (x, y, z)$ denotes the vector of Cartesian spatial coordinates, $(\cdot)'_{\infty,1}$ denotes the perturbations with respect to the mean free-stream quantities $\overline{(\cdot)}_{\infty,1}$ and '$c.c.$' stands for complex conjugate. The quantities $\mathbf{k}_j = (k_{x,j}, k_{y,j}, k_{z,j})$, ω_j, $\hat{p}_j$ and ϕ_j represent the wavenumber vector, angular frequency, complex amplitude and phase, respectively, of the plane acoustic wave with index j. The norm of the wavenumber vector is defined as $\|\mathbf{k}_j\| \equiv \sqrt{k^2_{x,j} + k^2_{y,j} + k^2_{z,j}}$. The angular frequency ω_j of the jth wave is related to its wavenumber $\mathbf{k}_j$ via the dispersion relation for acoustic waves (McKenzie & Westphal 1968)

$$\omega_j(\mathbf{k}_j) = \overline{\mathbf{u}}_{\infty,1} \cdot \mathbf{k}_j \pm \overline{c}_{\infty,1} \|\mathbf{k}_j.\|, \tag{A2}$$

so that corresponding group velocity $\overline{\mathbf{v}}_j$ can be written as

$$\overline{\mathbf{v}}_{\pm,j} \equiv \frac{\partial \omega_j}{\partial \mathbf{k}_j} = \overline{\mathbf{u}}_{\infty,1} \pm \overline{c}_{\infty,1} \left(\frac{\mathbf{k}_j}{\|\mathbf{k}_j\|} \right). \tag{A3}$$

The plus and minus signs ($\pm$) in (A3) correspond to a group velocity that is faster and slower, respectively, in comparison with the free-stream speed; however, relative to the mean free-stream velocity, both wave groups propagate at the speed of sound along the wavefront orientation $\mathbf{k}_j/\|\mathbf{k}_j\|$. Here, we follow the definition of McKenzie & Westphal (1968) by referring to acoustic waves with $\overline{\mathbf{v}}_{+,j} = \overline{\mathbf{u}}_{\infty,1} + \overline{c}_{\infty,1}(\mathbf{k}_j/\|\mathbf{k}_j\|)$ as the 'fast' acoustic waves and those with a group speed of $\overline{\mathbf{v}}_{-,j} = \overline{\mathbf{u}}_{\infty,1} - \overline{c}_{\infty,1}(\mathbf{k}_j/\|\mathbf{k}_j\|)$ as 'slow' acoustic waves.

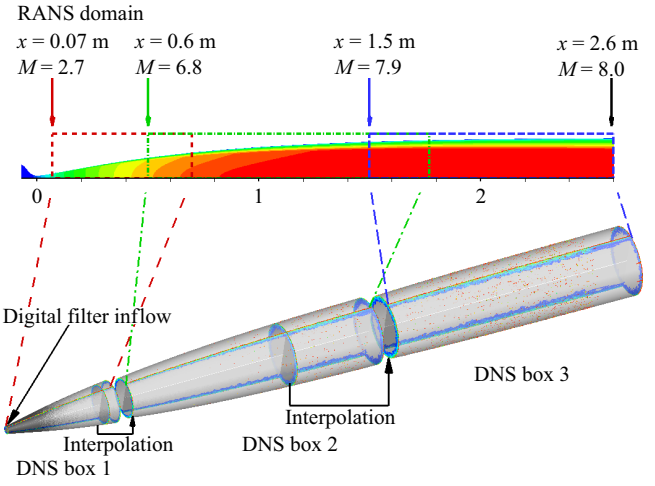

Figure 25. Computational domain set-up for the precursor DNS of the full-scale axisymmetric nozzle of Sandia HWT-8 (Duan *et al.* 2019*b*).

Given a tunnel operating condition with known values of time-averaged free-stream quantities, the information required to complete the specification of the acoustic field according to the plane-wave model in (A1) corresponds to the parameters $\mathbf{k}_j$, $\hat{p}_j$, ϕ_j and making a choice between fast and slow waves or a mixture thereof.

A.2 *Model parameter calibration*

To determine the unknown parameters required to synthesise the broadband field of 3-D acoustic disturbances in the free-stream region from the tunnel DNS, a precursor DNS of the full-scale axisymmetric nozzle of the Sandia HWT-8 was first conducted with an emphasis on characterizing the properties of free-stream acoustic disturbances in the test section of the tunnel. The simulated flow conditions fell within the range of tunnel operating conditions, with a total pressure of $P_0 = 4692$ kPa and a total temperature of $T_0 = 617$ K. Figure 25 shows the computational set-up of the precursor simulation of the Sandia HWT-8 for generating the tunnel acoustic field. It includes both Reynolds-averaged Navier–Stokes (RANS) computation over a larger domain and a DNS within a portion of that domain. The RANS domain started with the converging section upstream of the nozzle throat, which is located at $x \approx 0$ m. The diverging section spanned from $x \approx 0$ to $x \approx 2.6$ m, and was followed by the test section. The DNS domain started slightly downstream of the nozzle throat at $x = 0.07$ m with a local free-stream Mach number of $M_\infty = 2.7$, and ended at the nozzle exit at $x = 2.6$ m with a free-stream Mach number of $M_\infty \approx 8.0$. Additional details of the tunnel-noise simulation, including the validation of DNS against Sandia's experiment at the nozzle wall, can be found in Duan *et al.* (2019*b*). Figure 26 shows an instantaneous visualisation of the density gradient associated with the radiated acoustic field in the Sandia HWT-8. The prominent structures associated with acoustic fluctuations within the free-stream region exhibited a preferred orientation of $\theta \approx 20°$ with respect to the nozzle centreline within the streamwise–radial plane. The density gradients at a given axial location of the nozzle reveal the broad range orientations of the acoustic field, adding to the stochastic nature of the wavefront pattern.

Next, we extracted the instantaneous pressure field within a rectangular box from the free-stream region of the precursor DNS as shown in figure 27. The cross-plane dimensions of this rectangular box were chosen to be larger than the base

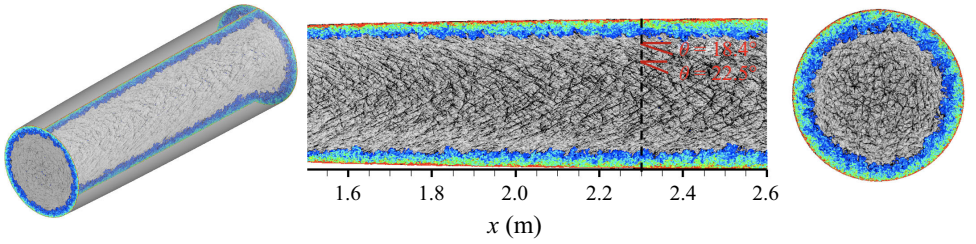

Figure 26. Numerical schlieren images (i.e. density gradient contours) of radiated acoustic waves within the nozzle of the Sandia HWT-8 (Duan *et al.* 2019*b*). The vertical dashed line indicates the axial location of the selected cross-section visualised in the right panel.

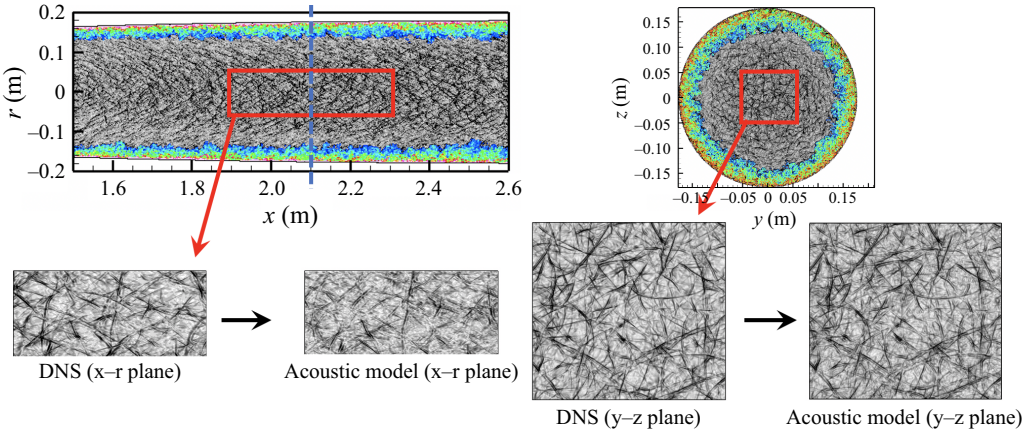

Figure 27. Schematic of the rectangular domain for extracting free-stream acoustic disturbances from the precursor DNS of an empty wind tunnel. The vertical dashed line indicates the streamwise location of the selected cross-plane visualised on the top right.

radius of the cone model and its axial extent spanned from $x = 1.82\,\mathrm{m}$ to $x = 2.23\,\mathrm{m}$, which is immediately upstream of where the cone is mounted within the tunnel. The size of the rectangular domain relative to the nozzle boundary-layer thickness was approximately $(L_x/\delta_{nozzle}, L_y/\delta_{nozzle}, L_z/\delta_{nozzle}) = (10.1, 4.6, 4.6)$ and included a total of (1200, 400, 400) points in the axial and the two transverse directions, respectively, from the precursor DNS. Here, $\delta_{nozzle} = 38.5\,\mathrm{mm}$ represents the nozzle-wall boundary-layer thickness at $x = 2.1\,\mathrm{m}$, which denotes the axial midpoint of the acoustic domain. The selected domain for acoustic wave extraction was large enough to accommodate the largest free-stream acoustic structures. Following a detrending process to compute the acoustic pressure fluctuations $p'_{\infty,1}$ relative to the mean pressure $\overline{p}_{\infty,1}$, spatial fast Fourier transforms (FFTs) were performed along each spatial direction of the rectangular domain. This provided the specification of the spectral content of the acoustic fluctuations, including the wavenumber vector $\mathbf{k}_j = (k_{x,j}, k_{y,j}, k_{z,j})$, complex amplitude $\hat{p}_j$ and the phase angle ϕ_j for each Fourier mode denoted by index j. Given the wavenumber vector $\mathbf{k}_j$ of each mode j, its frequency was computed by (A2) with the assumption of a slow acoustic wave. The dominance of slow acoustic waves in the free-stream of conventional supersonic and hypersonic tunnels had been suggested in multiple previous studies (Duan *et al.* 2014, 2016, 2019*a*; Goparaju *et al.* 2022), and is further confirmed in § A.3 for the current tunnel conditions. To guarantee that only statistically relevant modes are kept in the synthesised acoustic field, the 3-D spatial FFT was repeated within the same rectangular

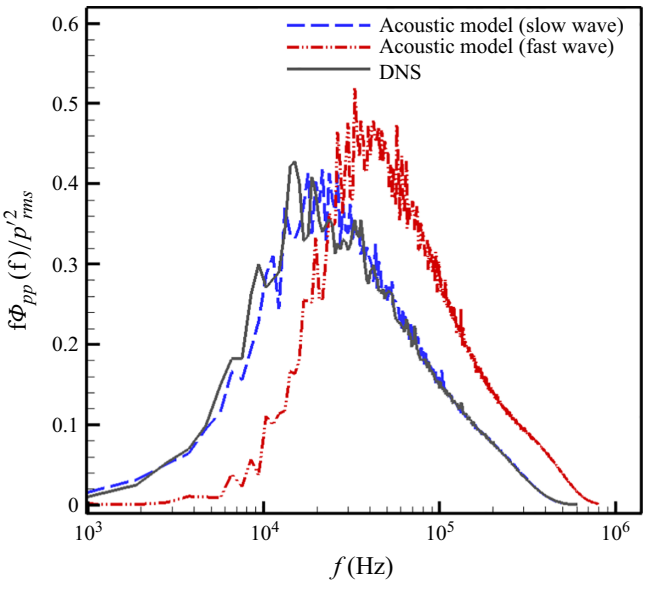

Figure 28. The PSD of free-stream acoustic disturbances computed based on the calibrated acoustic model of (A1) with fast (+) or slow (-) acoustic wave assumptions in comparison with that of the precursor tunnel DNS at $x \approx 2.1$ m.

domain for a total of 70 snapshots of the instantaneous free-stream acoustic fields. The modal amplitudes $\hat{p}_j$ in the acoustic model from (A1) were computed by using an average of the power spectra across the snapshots. To preserve the stochasticity of the reconstructed field, the phase angles (ϕ_j) in the acoustic model were derived from a single instantaneous snapshot of the extracted 3-D acoustic field.

We note that the extraction of the acoustic modes was performed in the Cartesian domain instead of the cylindrical coordinate used in the tunnel simulation. This allowed us to use the computationally efficient FFT libraries to speed up the mode extraction process rather than dealing with the more expensive Hankel transformations required for the cylindrical coordinate system. It also allows the tunnel-noise generation technique to be applied to hypersonic wind tunnels with a rectangular/square nozzle shape such as NASA's 20 Inch Mach 6 wind tunnel (Hildebrand *et al.* 2022, 2023).

A.3 *Assessment of model performances*

Figure 28 shows the PSD of free-stream acoustic disturbances based on the acoustic model from (A1) after calibration against the data from the precursor DNS. The acoustic model based on the slow-acoustic-wave assumption shows good agreement with the DNS data, reinforcing the conclusion that slow acoustic waves dominate the radiated noise from the nozzle-wall turbulent boundary layer.

Figure 29 shows the wavenumber spectra of free-stream acoustic disturbances based on the calibrated acoustic model from (A1). The results plotted herein include the comparison of spectral estimates for the extracted acoustic field based on several spatial domains with the spectra obtained from the precursor DNS of an empty tunnel. Here, the rectangular domain sizes as described in § A.1 are scaled by the local nozzle boundary-layer thickness δ_{nozzle} ($\delta_{nozzle} = 0.0385$ m at the reference axial location of $x \simeq 2.1$ m, where the radius of the local tunnel test section is approximately 0.177 m), and the wavenumber spectra of both pressure and streamwise velocity fluctuations have been included to show the

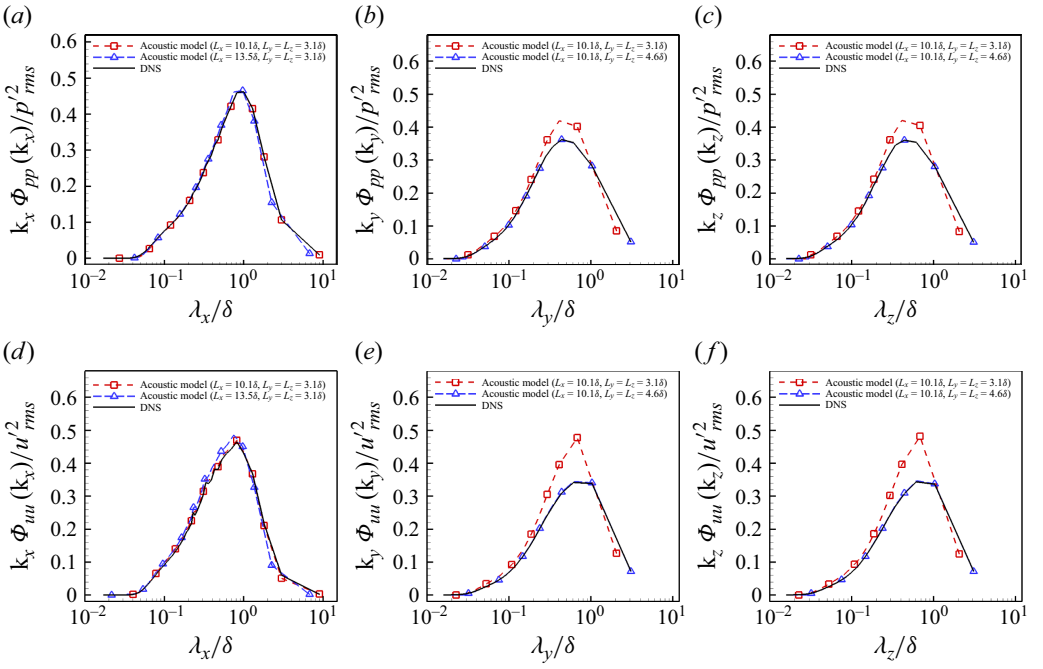

Figure 29. Wavenumber spectra of free-stream acoustic disturbances computed with the calibrated acoustic model of (A1) by using different spatial domain sizes in comparison with those of the precursor tunnel DNS. (*a–c*) Pressure and (*d–f*) streamwise velocity.

sensitivity of different acoustic quantities to the model parameters. With the selected domain size of $(L_x/\delta_{nozzle}, L_y/\delta_{nozzle}, L_z/\delta_{nozzle}) = (10.1, 4.6, 4.6)$ for extracting the free-stream acoustic waves, excellent comparisons between the model and the DNS are achieved in spectra of both pressure and velocity fluctuations. The figure also confirmed that a large enough domain size in the transverse directions is required for the modelled wavenumber spectra to match with the tunnel DNS data.

Figure 30 depicts instantaneous visualisations from the temporal evolution of free-stream acoustic disturbances in a cross-plane (i.e. $y-z$ plane) at the reference axial location of $x \simeq 2.1$ m. Results are shown both for the acoustic field predicted by the model from (A1) and its comparison with the corresponding snapshots from the precursor tunnel DNS. Here, the free-stream acoustic disturbances are visualised as numerical schlieren contours based on the density gradient. The visualisation at $t = 0$ s corresponds to the snapshot from which the modal phase angles ϕ_j of all the plane waves in the ansatz were derived, and the time delay was measured in terms of the integral time scale Λ of the free-stream pressure disturbances ($\Lambda = 5.8$ μs at $x \simeq 2.1$ m). The apparent similarity in the instantaneous acoustic structures between the model and DNS confirms that the free-stream acoustic disturbances generated from the acoustic model closely mimic those of the DNS over time intervals of at least $t = 9\Lambda$, which corresponds to at least 1.5 times the large-eddy turnover time $\delta_{nozzle}/U_{\infty,1}$ of the nozzle-wall boundary layer, while preserving the stochastic nature of the free-stream acoustic field.

A.4 *Effects of the wavenumber cutoff in the tunnel-noise model*

In the DNS study of BLT over a circular cone as shown in § 3, a low-pass wavenumber filter with a spectral cutoff of eight points per wavelength (PPW) was applied to remove

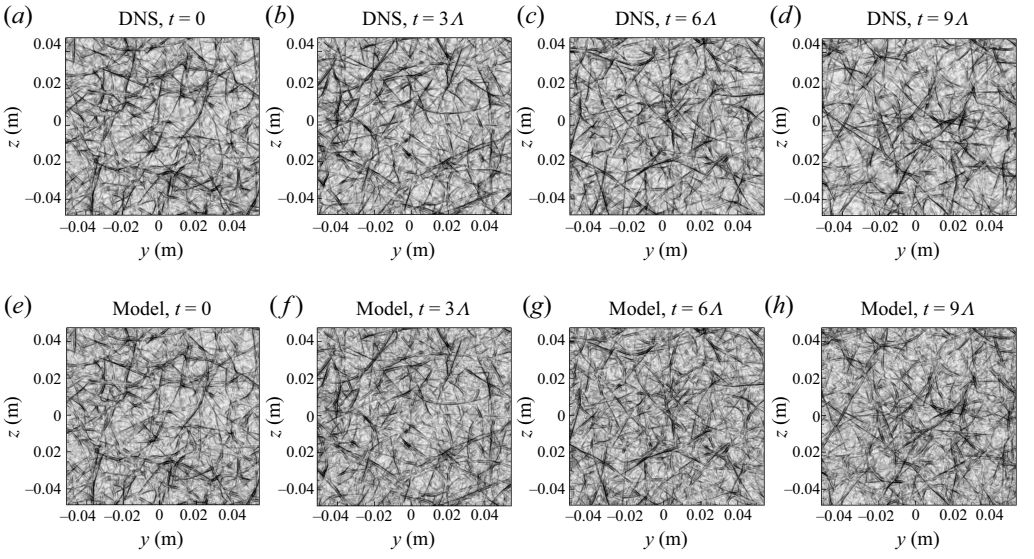

Figure 30. Temporal evolution of free-stream acoustic disturbances in a cross-plane ($y-z$ plane) at $x \simeq 2.1$ m, generated by the calibrated acoustic model of (A1) in comparison with those from the precursor tunnel DNS.

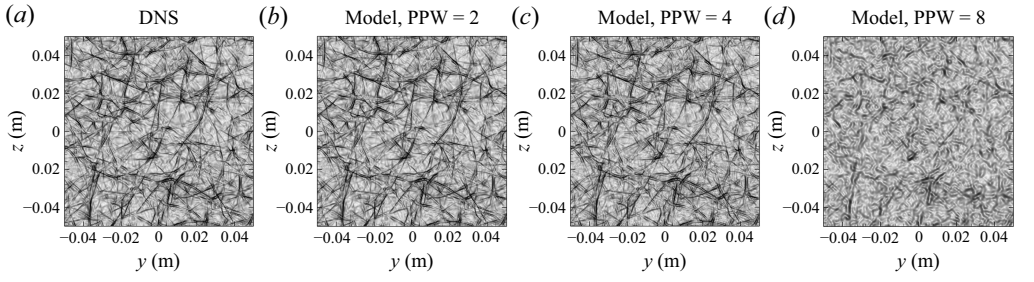

Figure 31. Comparison between the tunnel DNS and the acoustics model with a different spectral wavenumber cutoff at t = 0 s.

the small-wavelength waves that cannot be accurately resolved by the tunnel DNS, because the WENO scheme used for the tunnel simulation requires approximately eight PPW to accurately propagate a linear wave over multiple wavelengths (Brehm *et al.* 2015; Martín *et al.* 2006). The wavenumber cutoff reduced the total number of plane waves in the acoustic-wave ansatz by a factor of 64. Even with this large reduction of modes, the model has around 95 % of the total power spectrum of pressure fluctuation of the 3-D FFT.

Figure 31 highlights the variation in the instantaneous acoustic field as a function of cutoff PPW. We noted that large coherent structures in the free-stream noise field were maintained up to PPW = 8, while PPW = 2 (corresponding to no wavenumber cutoff) reproduced the DNS results. Even when modelling tunnel noise with a substantially reduced number of plane acoustic modes corresponding to PPW = 8, the cone DNS successfully reproduced most of the features of BLT measured by the experiment as shown in § 3.

References

Balakumar, P. & Chou, A. 2016 Transition prediction in hypersonic boundary layers using receptivity and free-stream spectra. *AIAA Paper* 2016-0847.

BALAKUMAR, P. & CHOU, A. 2018 Transition prediction in hypersonic boundary layers using receptivity and free-stream spectra. *AIAA J.* **56** (1), 193–208.
BALAKUMAR, P. & KEGERISE, M. 2011 Receptivity of hypersonic boundary layers to acoustic and vortical disturbances. *AIAA Paper* 2011-371.
BALAKUMAR, P. & KEGERISE, M.A. 2015 Receptivity of hypersonic boundary layer over straight and flared cones. *AIAA J.* **53** (8), 2097–2109.
BALAKUMAR, P., KING, R.A., CHOU, A., OWENS, L.R. & KEGERISE, M.A. 2018 Receptivity and forced response to acoustic disturbances in high-speed boundary layers. *AIAA J.* **56** (2), 510–523.
BECKWITH, I.E. 1975 Development of a high Reynolds number quiet tunnel for transition research. *AIAA J.* **13** (3), 300–306.
BECKWITH, I.E. & MILLER, C.G. 1991 Aerothermodynamics and transition in high-speed wind tunnels at NASA Langley. *Annu. Rev. Fluid Mech.* **22** (1), 419–439.
BOGEY, C., DE CACQUERAY, N. & BAILLY, C. 2011 Finite differences for coarse azimuthal discretization and for reduction of effective resolution near origin of cylindrical flow equations. *J. Comput. Phys.* **230** (4), 1134–1146.
BREHM, C., BARAD, M.F., HOUSMAN, J.A. & KIRIS, C.C. 2015 A comparison of higher-order finite-difference shock capturing schemes. *Comput. Fluids* **122**, 184–208.
BUSHNELL, D.M. 1990 Notes on initial disturbance fields for the transition problem. In *Instability and Transition* (ed. HUSSAINI M.Y. & VOIGT R.G.), vol. 1, pp. 217–232, Springer-Verlag.
CASPER, K.M. 2009 Hypersonic wind-tunnel measurements of boundary-layer pressure fluctuations. PhD thesis, Purdue University, USA.
CASPER, K.M., BERESH, S.J., HENFLING, J.F., SPILLERS, R.W., PRUETT, B.O.M. & SCHNEIDER, S.P. 2016 Hypersonic wind-tunnel measurements of boundary-layer transition on a slender cone. *AIAA J.* **54** (4), 1250–1263.
CASSANTO, J.M. & ROGERS, D.A. 1975 An experiment to determine nose tip transition with fluctuating pressure measurements. *AIAA J.* **13** (10), 1257–1258.
DRIEST, E.R.V. 1956*a* On turbulent flow near a wall. *J. Aeronaut. Sci.* **23** (11), 1007–1011.
DRIEST, E.R.V. 1965*b*, The problem of aerodynamic heating. *Aeronaut. Engng Rev.* **15** (10), 26–41.
DUAN, L., BEEKMAN, I. & MARTÍN, M.P. 2010 Direct numerical simulation of hypersonic turbulent boundary layers. Part 2: effect of wall temperature. *J. Fluid Mech.* **655**, 419–445.
DUAN, L., BEEKMAN, I. & MARTÍN, M.P. 2011 Direct numerical simulation of hypersonic turbulent boundary layers. Part 3: effect of Mach number. *J. Fluid Mech.* **672**, 245–267.
DUAN, L., CHOUDHARI, M.M. & WU, M. 2014 Numerical study of acoustic radiation due to a supersonic turbulent boundary layer. *J. Fluid Mech.* **746**, 165–192.
DUAN, L., CHOUDHARI, M.M. & ZHANG, C. 2016 Pressure fluctuations induced by a hypersonic turbulent boundary layer. *J. Fluid Mech.* **804**, 578–607.
DUAN, L. *et al.* 2019*a* Characterization of free-stream disturbances in conventional hypersonic wind tunnels. *J. Spacecr. Rockets* **56** (2), 357–368.
DUAN, L., NICHOLSON, G.L., HUANG, J., CASPER, K.M., WAGNILD, R.M. & BITTER, N.P. 2019*b* Direct numerical simulation of nozzle-wall pressure fluctuations in a Mach 8 wind tunnel. *AIAA Paper* 2019-0847.
EDELMAN, J.B., CHYNOWETH, B.C., MCKIERNAN, G.R., SWEENEY, C.J. & SCHNEIDER, S.P. 2016 Instability measurements in the Bboeing/AFOSR Mach-6 quiet tunnel. *AIAA Paper* 2016-3343.
FEDOROV, A.V. 2011 Transition and stability of high-speed boundary layers. *Annu. Rev. Fluid Mech.* **43** (1), 79–95.
FRANKO, K.J. & LELE, S.K. 2013 Breakdown mechanisms and heat transfer overshoot in hypersonic zero pressure gradient boundary layers. *J. Fluid Mech.* **730**, 491–532.
GIBIS, T., SCIACOVELLI, L., KLOKER, M. & WENZEL, C. 2024 Heat-transfer effects in compressible turbulent boundary layers–a regime diagram. *J. Fluid Mech.* **995**, A14.
GOPARAJU, H., LIU, Y., DUAN, L. & GAITONDE, D.V. 2022 Supersonic transition induced by numerical tunnel disturbances. *AIAA Paper* 2022-1826.
GOPARAJU, H., UNNIKRISHNAN, S. & GAITONDE, D.V. 2021 Effects of nose bluntness on hypersonic boundary-layer receptivity and stability. *J. Spacecr. Rockets* **58** (3), 1–17.
HADER, C. & FASEL, H.F. 2016 Laminar-turbulent transition on a flared cone at Mach 6. *AIAA Paper* 2016-3344.
HADER, C. & FASEL, H.F. 2017 Fundamental resonance breakdown for a flared cone at Mach 6. *AIAA Paper* 2017-0765.
HADER, C. & FASEL, H.F. 2018 Towards simulating natural transition in hypersonic boundary layers via random inflow disturbances. *J. Fluid Mech.* **847**, R3.

HILDEBRAND, N., CHOUDHARI, M.M., DEEGAN, C.P., HUANG, J. & DUAN, L. 2022 Direct numerical simulation of acoustic disturbances in a hypersonic two-dimensional nozzle configuration. *AIAA J.* **60** (6), 3452–3463.

HILDEBRAND, N., CHOUDHARI, M.M. & DUAN, L. 2023 Reynolds-number effects on the acoustic disturbance environment in a Mach 6 nozzle. *AIAA J.* **61** (11), 4783–4796.

HUANG, J., DUAN, L., CASPER, K.M., WAGNILD, R.M. & BITTER, N.P. 2020 Direct numerical simulation of turbulent pressure fluctuations over a cone at Mach 8. *AIAA Paper* 2020-1065.

HUANG, J., DUAN, L., CASPER, K.M., WAGNILD, R.M. & BITTER, N.P. 2024 Transducer resolution effect on pressure fluctuations beneath hypersonic turbulent boundary layers. *AIAA J.* **62** (3), 882–895.

HUANG, J., DUAN, L. & CHOUDHARI, M.M. 2022 Direct numerical simulation of hypersonic turbulent boundary layers: effect of spatial evolution and Reynolds number. *J. Fluid Mech.* **937**, A3.

HUANG, J., DUAN, L., L, & CHOUDHARI, M.M. 2017*a* Direct numerical simulation of acoustic noise generation from the nozzle wall of a hypersonic wind tunnel. *AIAA Paper* 2017-3631.

HUANG, J., ZHANG, C., DUAN, L. & CHOUDHARI, M.M. 2017*b* Direct numerical simulation of hypersonic turbulent boundary layers inside an axisymmetric nozzle. *AIAA Paper* 2017-0067.

JIANG, G.S. & SHU, C.W. 1996 Efficient implementation of weighted ENO schemes. *J. Comput. Phys.* **126** (1), 202–228.

JOHNSON, R., MACOUREK, M. & SAUNDERS, H. 1969 Boundary layer acoustic measurements in transitional and turbulent flow at M infinity equals 4.0. *AIAA Paper* 2011-3432.

KARA, K., BALAKUMAR, P. & KANDIL, O.A. 2011 Effects of nose bluntness on hypersonic boundary-layer receptivity and stability over cones. *AIAA J.* **49** (12), 2593–2606.

KENDALL, J.M. 1975 Wind tunnel experiments relating to supersonic and hypersonic boundary-layer transition. *AIAA J.* **13** (3), 290–299.

KENNEDY, R., JEWELL, J., PAREDES, P. & LAURENCE, S. 2022 Characterization of instability mechanisms on sharp and blunt slender cones at Mach 6. *J. Fluid Mech.* **936**, A39.

KEYES, F.G. 1951 A summary of viscosity and heat-conduction data for He, A, H_2, O_2, CO, CO_2, H_2O. *Trans. Am. Soc. Mech. Engrs* **73**, 589–596.

LADERMAN, A.J. 1977 Review of wind-tunnel free-stream pressure fluctuations. *AIAA J.* **15** (4), 605–608.

LAUFER, J. 1961 Aerodynamic noise in supersonic wind tunnels. *J. Aerosp. Sci.* **28** (9), 685–692.

LAUFER, J. 1964 Some statistical properties of the pressure field radiated by a turbulent boundary layer. *Phys. Fluids* **7** (8), 1191–1197.

LITTON, D.K., EDWARDS, J.R. & WHITE, J.A. 2003 Algorithmic enhancements to the VULCAN Navier–Stokes solver. *AIAA Paper* 2003-3979.

LIU, Y. & DUAN, L. 2022 Interaction of a tunnel-like acoustic disturbance field with a normal shock wave: theory and simulation. *AIAA Paper* 2022-3410.

LIU Y., SCHUABB M., DUAN L., PAREDES P. & CHOUDHARI M.M. 2022 Interaction of a tunnel-like acoustic disturbance field with a blunt cone boundary layer at Mach 8. *AIAA Paper* 2022-3250.

MA, Y. & ZHONG, X. 2003 Receptivity of a supersonic boundary layer over a flat plate. Part 1. Wave structures and interactions. *J. Fluid Mech.* **488**, 31–78.

MACK, L.M. 1975 Linear stability theory and the problem of supersonic boundary-layer transition. *AIAA J.* **13** (3), 278–289.

MAHESH, K., LEE, S., LELE, S.K. & MOIN, P. 1995 The interaction of an isotropic field of acoustic waves with a shock wave. *J. Fluid Mech.* **300**, 383–407.

MALIK, M., SPALL, R. & CHANG, C.-L. 1990 Effect of nose bluntness on boundary layer stability and transition. *AIAA Paper* 1990-112.

MARINEAU, E.C., GROSSIR, G., WAGNER, A., LEINEMANN, M., RADESPIEL, R., TANNO, H., CHYNOWETH, B.C., SCHNEIDER, S.P., WAGNILD, R.M. & CASPER, K.M. 2019 Analysis of second-mode amplitudes on sharp cones in hypersonic wind tunnels. *J. Spacecr. Rockets* **56** (2), 307–318.

MARTELLUCCI, A., CHAUMP, L., ROGERS, D. & SMITH, D. 1973 Experimental determination of the aeroacoustic environment about a slender cone. *AIAA J.* **11** (5), 635–642.

MARTÍN, M.P., TAYLOR, E.M., WU, M. & WEIRS, V.G. 2006 A bandwidth-optimized WENO scheme for the direct numerical simulation of compressible turbulence. *J. Comput. Phys.* **220** (1), 270–289.

MCKENZIE, J.F. & WESTPHAL, K.O. 1968 Interaction of linear waves with oblique shock waves. *Phys. Fluids* **11** (11), 2350–2362.

MOHSENI, K. & COLONIUS, T. 2000 Numerical treatment of polar coordinate singularities. *J. Comput. Phys.* **157** (2), 787–795.

PATE, S.R. & BROWN, M.D. 1969 Acoustic measurements in supersonic transitional boundary layers, Tech. Rep. AEDC-TR-69-182, Arnold Engineering Development Center.

PATE, S.R. 1978 Dominance of radiated aerodynamic noise on boundary-layer transition in supersonic-hypersonic wind tunnels, Tech. Rep. AEDC-TR-77-107, Arnold Engineering Development Center.
PATE, S.R. 1980 Effects of wind tunnel disturbances on boundary-layer transition with emphasis on radiated noise: a review. *AIAA Paper* 1980-0431.
PIROZZOLI, S. & BERNARDINI, M. 2011 Turbulence in supersonic boundary layers at moderate Reynolds numbers. *J. Fluid Mech.* **688**, 120–168.
PRIEBE, S. & MARTIN, P. 2011 Direct numerical simulation of a hypersonic turbulent boundary layer on a large domain. *AIAA Paper* 2011-3432.
RAN, W., ZARE, A., HACK, M.J.P. & JOVANOVIĆ, M.R. 2019 Stochastic receptivity analysis of boundary layer flow. *Phys. Rev. Fluids* **4** (9), 093901.
SCHLATTER, P. & ÖRLÜ, R. 2010 Assessment of direct numerical simulation data of turbulent boundary layers. *J. Fluid Mech.* **659**, 116–126.
SCHNEIDER, S.P. 2001 Effects of high-speed tunnel noise on laminar-turbulent transition. *J. Spacecr. Rockets* **38** (3), 323–333.
SCHNEIDER, S.P. 2008 Development of hypersonic quiet tunnels. *J. Spacecr. Rockets* **45** (4), 641–664.
SCHNEIDER, S.P. 2015 Developing mechanism-based methods for estimating hypersonic boundary-layer transition in flight: the role of quiet tunnels. *Prog. Aerosp. Sci.* **72**, 17–29.
SCHOPPER, M.R. 1984 Interaction of aerodynamic noise with laminar boundary layers in supersonic wind tunnels, Tech. Rep, NASA.
SCHUABB, M., DUAN, L., SCHOLTEN, A., PAREDES, P. & CHOUDHARI, M.M. 2024 Hypersonic boundary-layer transition over a blunt circular cone in a Mach 8 digital wind tunnel. *AIAA Paper* 2024-2181.
SMITH, J.A., DECHANT, L.J., CASPER, K.M., MESH, M. & FIELD, R.V., Jr 2016 Comparison of a turbulent boundary layer pressure fluctuation model to hypersonic cone measurements. *AIAA Paper* 2016-4047.
STEMMER, C., KLOKER, M., RIST, U. & WAGNER, S. 1999 DNS of point-source induced transition in an airfoil boundary-layer flow. In *High Performance Computing in Science and Engineering'98: Transactions of the High Performance Computing Center Stuttgart (HLRS) 1998*, pp. 213–222, Springer.
STETSON, K. 1983 Nosetip bluntness effects on cone frustum boundary layer transition in hypersonic flow. *AIAA Paper* 1983-1763.
THOMPSON, K.W. 1987 Time dependent boundary conditions for hyperbolic systems. *J. Comput. Phys.* **68** (1), 1–24.
WASON, M.P. 2019 Calibration of high-frequency pressure sensors using low-pressure shock waves. PhD thesis, Purdue University, West Lafayette, IN.
WHITE, F.M. & CORFIELD, I. 2006 Viscous fluid flow, vol. 3, McGraw-Hill New York.
WILLIAMS, O.J.H., SAHOO, D., BAUMGARTNER, M.L. & SMITS, A.J. 2018 Experiments on the structure and scaling of hypersonic turbulent boundary layers. *J. Fluid Mech.* **834**, 237–270.
WILLIAMSON, J.H. 1980 Low-storage Runge-Kutta schemes. *J. Comput. Phys.* **35** (1), 48–56.
ZHONG, X. & MA, Y. 2006 Boundary-layer receptivity of Mach 7.99 flow over a blunt cone to free-stream acoustic waves. *J. Fluid Mech.* **556**, 55.
ZHONG, X. & WANG, X. 2012 Direct numerical simulation on the receptivity, instability, and transition of hypersonic boundary layers. *Annu. Rev. Fluid Mech.* **44** (1), 527–561.